Effects of complex terrain on the shortwave radiative balance : A sub–grid scale parameterization for the GFDL Land Model version 4.1

Enrico Zorzetto[1], Sergey Malyshev[2], Nathaniel Chaney[3], David Paynter[2], Raymond Menzel[2, 4], and Elena Shevliakova[2]

[1]Program in Atmospheric and Oceanic Sciences, Princeton University, Princeton, NJ, USA
[2]NOAA OAR Geophysical Fluid Dynamics Laboratory, Princeton, NJ, USA
[3]Department of Civil and Environmental Engineering, Duke University, Durham, NC, USA
[4]University Corporation for Atmospheric Research, Princeton, NJ, USA

Correspondence: Enrico Zorzetto (ez6263@princeton.edu)

Abstract.

Parameterizing incident solar radiation over complex topography regions in Earth System Models (ESMs) remains a challenging task. In ESMs, downward solar radiative fluxes at the surface are typically computed using plane parallel radiative transfer schemes, which do not explicitly account for the effects of a three-dimensional topography, such as shading and reflections. To improve the representation of these processes, we introduce and test a parameterization of radiation-topography interactions tailored to the Geophysical Fluid Dynamics Laboratory (GFDL) ESM land model. The approach presented here builds on an existing correction scheme for direct, diffuse and reflected solar irradiance terms over three-dimensional terrain. Here we combine this correction with a novel hierarchical multivariate clustering algorithm which explicitly describes the spatially varying downward irradiance over mountainous terrain. Based on a high-resolution digital elevation model, this combined method first defines a set of sub–grid land units ("tiles") by clustering together sites characterized by similar terrain-radiation interactions (e.g., areas with similar slope orientation, terrain and sky view factors). Then, based on terrain parameters characteristic for each tile, correction terms are computed to account for the effects of local 3-D topography on shortwave radiation over each land unit. We develop and test this procedure based on a set of Monte Carlo ray tracing simulations approximating the true radiative transfer process over three dimensional topography. Domains located in three distinct geographic regions (Alps, Andes, and Himalaya) are included in this study to allow for independent testing of the methodology over surfaces with differing topographic features. We find that accounting for the sub–grid spatial variability of solar irradiance originating from interactions with complex topography is important as these effects lead to significant local differences with respect to the plane-parallel case, as well as with respect to grid–cell scale average topographic corrections. We further quantify the importance of the topographic correction for a varying number of terrain clusters and for different radiation terms (direct, diffuse, and reflected radiative fluxes) in order to inform the application of this methodology in different ESMs with varying sub-grid tile structure. We find that even a limited number of sub–grid units such as 10, can lead to recovering more than 60% of the spatial variability of solar irradiance over a mountainous area.

1 Introduction

25 The presence of three-dimensional topography exerts an important control on the amount of solar radiation received by land. Over complex terrain, the incoming solar beam does not only undergo scattering and absorption within the atmospheric column, but is further modulated by the relative orientation of land surfaces, as well as by the potential shading and reflection effects by neighbouring slopes (Sirguey, 2009; Lenot et al., 2009; Lamare et al., 2020; Picard et al., 2020). The effect of surface roughness was recently shown to have important effects over snow covered surfaces, leading to a net decrease in surface reflectivity (Larue

30 et al., 2020).

Together, these effects lead to a spatially heterogeneous distribution of the radiative fluxes received by the surface. In turn, this heterogeneity can have important consequences for the local energy and water balance, and interact with other spatially–varying land processes such as evaporation (Brutsaert, 2013), snow melting (McCabe and Clark, 2005; Bales et al., 2006; Sirguey et al., 2009) and vegetation dynamics (Granger and Schulze, 1977; Gu et al., 2002).

35 Representing these processes at increasingly fine scales is the goal of state-of-the-art land components of Earth System Models (ESMs) (i.e., land models). However, global circulation models (GCMs) routinely compute shortwave radiative fluxes based on plane-parallel (PP) radiative transfer schemes which do not account for the effect of topography. This discrepancy poses a challenge for adequately capturing sub–grid scale processes in land models.

Several models have been proposed to account for the interaction of downward solar irradiance with complex topography,

40 accounting for slope orientation and shading effects (Isard, 1986; Hay and McKay, 1985; Duguay, 1993) as well as for the effect of surrounding slopes (Dozier, 1980; Dubayah et al., 1990; Dozier and Frew, 1990).

A recently developed radiation parameterization was developed to predict radiative fluxes over mountainous terrain via multiple linear regression (Chen et al., 2006; Lee et al., 2011). This approach (henceforth termed LLH) links flux corrections over mountains to a set of grid-cell average terrain variables which summarize the three-dimensional nature of the land surface and

45 are used as predictors for shortwave fluxes. The LLH parameterization for shortwave radiation over mountains has been implemented in Global Climate Models (GCMs) and the Weather Research and Forecasting (WRF) model; it has been extensively tested over the Tibetan plateau and the Western United States (Liou et al., 2007; Essery and Marks, 2007; Gu et al., 2012; Lee et al., 2013, 2015, 2019).

However, it is expected that sub–grid variability of these topographic effects may play a relevant role given the heterogeneous

50 nature of surface reflectivity and topographic features at scales smaller than the typical GCM grid cell. The importance of accounting for sub grid–scale topography when correcting shortwave radiative fluxes over mountains was recently pointed out by an application of LLH to the DOE E3SM Exascale Earth System Model, varying model resolution over a range of scales relevant for land processes (Hao et al., 2021).

This problem is especially relevant since in recent years the development of land models has increasingly been focusing on

55 the description of sug–grid variability of terrain properties (Tesfa and Leung, 2017; Chaney et al., 2018). For example, in the

current iteration of the GFDL land model, this objective is achieved by summarizing grid cell heterogeneity in sets of land units (termed "tiles") characterized by approximately homogeneous physical features (Shevliakova et al., 2009; Milly et al., 2014; Zhao et al., 2018; Dunne et al., 2020), including elevation, land cover, soil properties, and other environmental variables (Chaney et al., 2018). In the GFDL land model such a sub-grid representation has not been yet tailored to describing the interaction of shortwave radiation with topography. The objective of this work is bridging this discrepancy and developing a sub–grid parameterization for the effects of radiation over complex topography in the GFDL land model.

The sub–grid model structure is constructed using a hierarchical multivariate clustering approach (Chaney et al., 2016, 2018) to partition land domains in a set of clusters or *tiles*. Tiles are here defined as land units characterized by homogeneous topographic effects with respect to downward shortwave radiation. Thus, the terrain variables used for clustering land surfaces encode the physical mechanisms determining the spatial variability of radiative fluxes, such as shading and reflection from nearby slopes.

This clustering approach provides a parsimonious way to include high-resolution terrain information in global ESM simulations while limiting the number of sub–grid element employed. For each terrain tile, characterized by homogeneous terrain properties, we then develop an average correction to the downward solar fluxes to account for the effects of local topography. This approach thus bridges the gap between the scale at which radiation and other physical processes are represented in the GFDL ESM, and allows to study how the sub-grid heterogeneity of these processes impacts the long term evolution of the coupled physical system.

In the following, we present this new methodology and test it over three mountainous sites located in different geographic regions (Alps, Andes, Himalayas), showing how model resolution and number of tiles impact the performance of the methodology. Given the wide range of spatial scale involved in the description of sub–grid topography, we evaluate the performance of the parameterization across scales, focusing in particular on the possible nonlinear dependence of incident radiation on topographic features, and validating the model over independent sites.

The paper is organized as follows: we first review the existing parameterization for radiation over rugged terrain (Lee et al., 2011), and tailor it to our problem. This in turn requires training a model to predict topography-driven corrections for radiative fluxes based on terrain properties. Finally, we present the clustering algorithm used to divide the domain study in tiles, so as to compute local flux corrections over homogeneous regions.

The approach is then validated using different domains for independent training and testing of the methodology (Sec. 3.2), exploring the effects of terrain resolution and possible consequences of nonlinear radiation-topography interactions. Finally, we explore how different tiling structures with increasing resolution improve the representation of the spatially varying radiation fields over mountains (Sec. 3.4). We close by discussing assumptions and limitations of the proposed methodology, and suggesting future developments.

2 Methods

In order to properly account for the effects of land heterogeneity on the radiative transfer in ESMs, key variables must be obtained from high-resolution terrain data sets and properly summarized in order to capture their fine-scale effects on shortwave radiation fluxes. To this end, here we start by defining the radiative and terrain variables used to predict radiation over 3D topography. Then, we describe (i) the Monte Carlo ray tracing algorithm used for training and testing the predictive model, (ii) the terrain clustering algorithm used to classify land units based on the local topographic effects on radiation fluxes, and (iii) the predictive models used to link terrain properties to radiative fluxes in each land cluster. Together, these three steps provide a framework for computing fine-scale corrections to the shortwave radiation received by sub–grid land units in the GFDL land model.

2.1 Characterizing shortwave radiation over mountainous terrain

A parameterization explicitly accounting for the effects of 3D topography on the shortwave radiation budget was proposed by Lee et al. (2011) based on the results of Monte Carlo photon tracing simulations (Chen et al., 2006). Here we adopt a similar approach and, following the formalism introduced by Lee et al. (2011), classify the shortwave radiation incident at a target point at the surface into 5 distinct components: The direct and diffuse downward solar fluxes (F_{dir} and F_{dif}), and their terrain-reflected counterparts (F_{rdir}, F_{rdif}), which represent respectively direct beam or diffuse photons reaching the target site after a single reflection from neighbouring terrain. Finally, a coupled flux component (F_{coup}) consists of photons first reflected by the surface, and then either back-scattered by the atmosphere or reflected multiple times by the surface before reaching the target site. For a flat surface $F_{rdir}, F_{rdif} = 0$ while $F_{dir}, F_{dif}, F_{coup} \neq 0$ in general. We note that in the GFDL land model, diffuse radiation received by a flat surface with albedo α ($F_{dif,[LM|\alpha]}$) corresponds here to the sum of F_{dif} and F_{coup}. We note that these quantities can be computed separately by computing first the diffuse flux corresponding to a black surface ($F_{dif,[LM|\alpha=0]}$), case in which the coupled flux is zero, and by then computing the coupled flux for the actual land surface as $F_{coup} = F_{dif,[LM|\alpha]} - F_{dif,[LM,\alpha=0]}$. Conversely, the diffuse flux can be obtained as $F_{dif} = F_{dif,[LM|\alpha=0]}$. Based on this formalism, the normalized flux differences between the traditional plane-parallel (PP) case and the topography-aware case (3D) are the quantities object of our analysis which can be used to correct the shortwave radiative balance in ESMs. Following Lee et al. (2011), these quantities are expressed as

$$f_{dir} = \frac{F_{dir}^{(3D)} - F_{dir}^{(PP)}}{F_{dir}^{(PP)}}; \quad f_{dif} = \frac{F_{dif}^{(3D)} - F_{dif}^{(PP)}}{F_{dif}^{(PP)}}; \quad f_{rdir} = \frac{F_{rdir}^{(3D)}}{F_{dir}^{(PP)}}; \quad f_{rdif} = \frac{F_{rdif}^{(3D)}}{F_{dif}^{(PP)}}; \quad f_{coup} = \frac{F_{coup}^{(3D)} - F_{coup}^{(PP)}}{F_{coup}^{(PP)}} \quad (1)$$

where the reflected-direct and -diffuse components are normalized with respect to the corresponding non-reflected flux component since they are equal to zero in the plane-parallel case (Lee et al., 2011). These quantities are defined in Eq. (1) for a given surface albedo value. While direct and diffuse component are independent of surface albedo, the reflected flux components are linearly dependent on albedo. Finally, the coupled flux is nonlinearly dependent on surface albedo. A schematic representation of these flux components is reported in Figure 1. Predicting these five f_i terms over land tiles representing
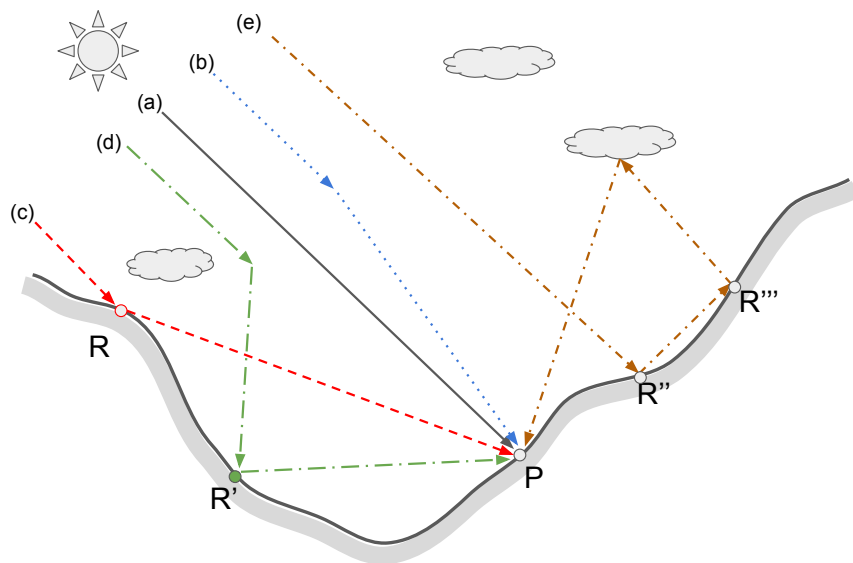
Figure 1. Conceptual representation of the five flux components used to characterize the nature of downward shortwave fluxes over rugged terrain, following the formalism used by Chen et al. (2006) and Lee et al. (2011). The figure includes the direct radiation flux (a), and diffuse radiation (b), consisting of photons which are absorbed at the surface target P after undergoing atmospheric scattering. Direct-reflected (c), and diffuse-reflected (d) fluxes represent photons which are reflected once at the surface. Finally, the coupled (e) flux component include light undergoing multiple reflections at the surface, or reflection at the surface and then atmospheric scattering. For all components, the figure shows paths incident at a point P at the surface.

heterogeneous terrain properties is the objective here. To this end, a predictive model linking the f_i's to tile terrain properties is necessary. To train such a model we use ray tracing simulations which are discussed next.

2.2 A Monte Carlo Ray tracing algorithm

Due to the complex interactions involved, topographic effects on shortwave radiation are generally studied based on Monte Carlo (MC) ray tracing techniques, which approximate the three dimensional radiative transfer process by tracking the fate of a large number of photons (Miesch et al., 1999; Chen et al., 2006; Mayer et al., 2010).

Here, in order to develop a predictive model for the 3D radiation correction terms, we employed a MC algorithm (sometimes referred to as photon tracing or ray tracing algorithm) to approximate the true physics of radiation–topography interactions. These high-resolution simulations are used to calibrate the predictive models for topographic effects over each tile, and to validate the proposed parameterization. The MC scheme explicitly describes the interaction of downwelling shortwave radiation with a 3D surface corresponding to a region characterized by complex topography. The algorithm was implemented in a software package which is made available in the online supplementary material. The MC method has been widely used to study radiation interaction with 3D surfaces (Chen et al., 2006; Lee et al., 2011; Mayer, 2009; Mayer et al., 2010; Villefranque
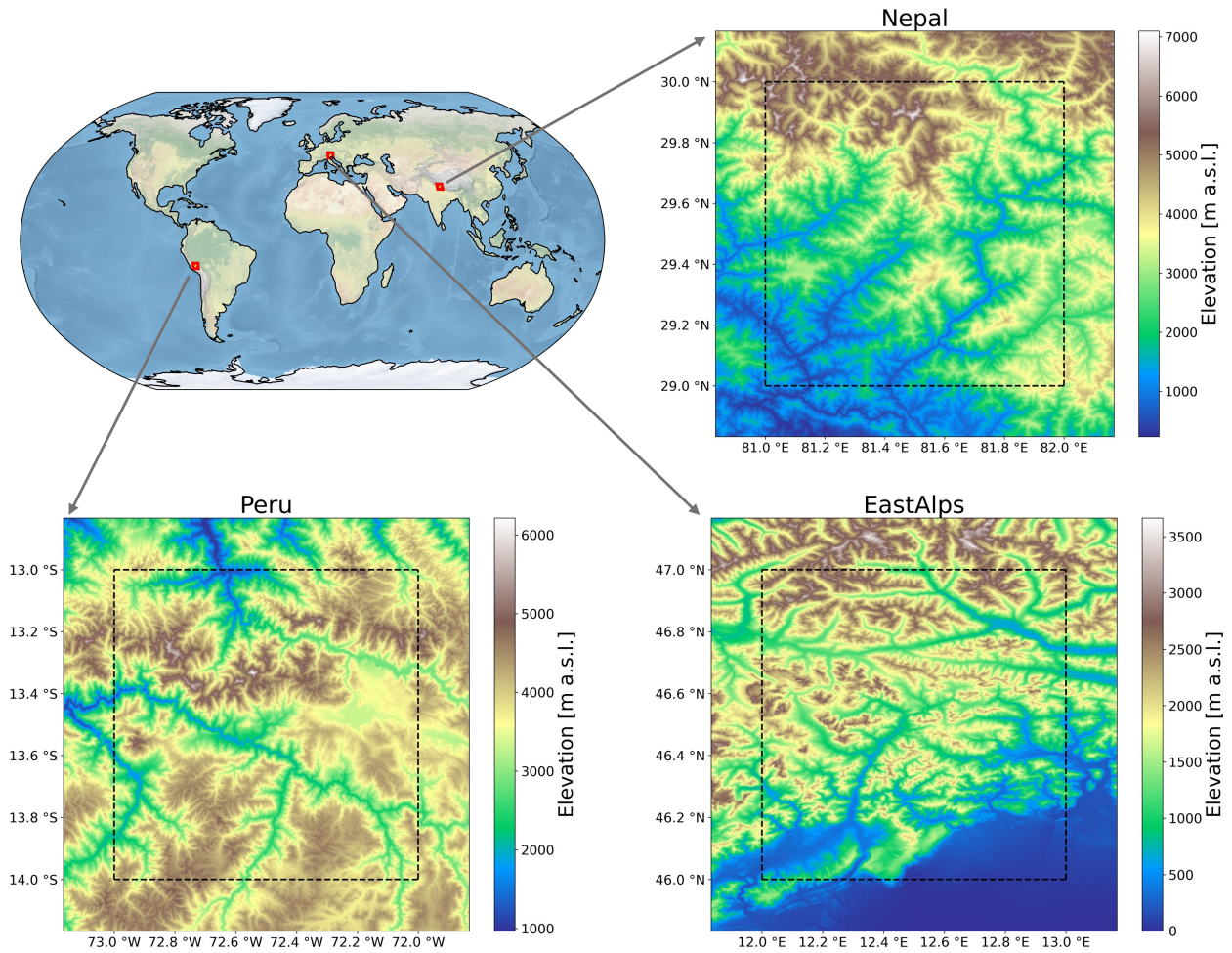
Figure 2. Location of the three land domains selected for this study. For each location, the 90-meters resolution digital elevation used in the study is shown.

et al., 2019; Larue et al., 2020). The MC model adopted here broadly follows previous models developed by Chen et al. (2006) and Mayer (2009).

In our MC algorithm, photons are randomly released at the top of atmosphere (TOA) and travel in a direction determined by the Sun's zenith θ_0 and azimuth ϕ_0 angles. After a path of random length, which depends on the optical properties of the medium, the photon encounters scattering or absorption based on the single scattering albedo properties of the atmospheric constituents (Fu and Liou, 1992; Liou, 2002). In the present simulation, we used for each site optical properties computed from the RRTMGP radiation code (Pincus et al., 2019) using the GFDL AM4 model (Zhao et al., 2018). We note that the Monte Carlo model is run offline, prescribing the atmospheric profile and solar position in each model run. The atmospheric column

135

used in the model is composed of 34 layers characterized by optical properties which encode the absorption and Rayleigh scattering of photons by gas molecules. We limit our analysis to aerosol-free and clear sky conditions, similar to previous studies (Chen et al., 2006; Lee et al., 2011). Therefore, atmospheric properties are completely determined by optical depths and single scattering albedo at each level (Liou, 2002). The lower boundary of the simulation domain is derived from high-resolution (90 m) terrain model derived from the Shuttle Radar Topography Mission (SRTM) dataset (Farr et al., 2007). SRTM elevation fields are used to construct a three–dimensional surface characterized by triangular mesh elements characterized by uniform albedo and Lambertian reflection. In the following we refer to "pixel" as the image elements of the high resolution input digital elevation maps, to clarify the difference with land model grid cell and land model sub-grid units, termed "tiles" in the following.

In each MC simulation, photons are tracked from the TOA until they are absorbed or leave the simulation domain. For each photon, interactions with atmospheric constituents (scattering or absorption) and with land surface elements (absorption or reflection) are used to characterize the nature of radiation incident over surface elements. Tracking the path of each photon, the downward irradiance is then decomposed into the 5 flux terms introduced in Section 2.1. If E_0 is the radiation incident at the TOA with a cosine of the zenith angle $\mu_0 = \cos\theta_0$, then the horizontal distribution of solar irradiance received by the land surface is given by (Mayer, 2009)

$$E_{k,l} = E_0 \cos\theta_0 \frac{1}{N} \frac{A}{A_{k,l}} \sum_{i=1}^{N_{k,l}^{(s)}} w_i \tag{2}$$

where w_i is the energy of the i-th incident photon, N is the total number of photons tracked in the simulation over a domain with area A, and $N_{k,l}^{(s)}$ is the number of photons absorbed by the surface within grid cell (k,l) with area horizontal plane surface area $A_{k,l}$. Photon are released with unit energy at the TOA, and lose a fraction of this energy through absorption in each atmospheric layer (Mayer, 2009), or through absorption at the ground. Therefore, Eq. (2) evaluates the spatial distribution of solar irradiance based on the density of photons that are absorbed at the surface. While a 3D mesh is used in the Monte Carlo simulations, the area of the cell $A_(k,l)$ is defined as the area of the cell on the horizontal plane. Equation (2) expresses the radiation received by a single land surface cell as a fraction of the radiation flux at the top of the surface E_0 by summing the energy w_i of all the photons absorbed by the surface over that area. Since the interactions of each photon are tagged (e.g., keeping track of atmospheric scattering and any previous reflections at the surface) the radiation received can be directly classified in one of the 5 flux components as defined in Eq. (1).

For two independent domains located in the Alps and Peru (Figure 2), the MC calculations were repeated for 6 solar zenith angle values ($\cos\theta_0 \in \{0.1, 0.25, 0.4, 0.55, 0.7, 0.85\}$), 4 solar azimuth angles ($\phi_0 \in \{0, \pi/2, \pi, 3\pi/2\}$), and a uniform surface reflectivity value set to $\alpha_s = 0.3$. While only two domains are used for MC calculations due to the computational expense of this procedure, an additional domain located in high mountain Asia (Figure 2) is used to further test the results of the spatial clustering over areas with different topographic features.

2.3 Predicting radiative fluxes over complex terrain

Over mountainous regions, the local irradiance at the surface can exhibit significant departures from its areal-average value at spatial scales routinely resolved in ESMs due to the complexity of topography and surface properties. In order to develop a simple parameterization to explain the magnitudes of these departures over mountains areas, we need predictor variables encoding the interaction between downward radiation and topographic features. To this purpose, we define here a set of relevant variables following previous work by Chen et al. (2006) and Lee et al. (2011). The terrain variables used to predict downward fluxes are i) the sky view factors V_d, which represents the ratio of diffuse sky irradiance at a point to that on an unobstructed horizontal surface, under the assumption of isotropic diffuse radiation.(Dozier and Frew, 1990; Helbig et al., 2009), ii) the terrain configuration C_t, which quantifies the contribution to the irradiance at a point originated by reflections from surrounding mutually visible slopes; iii) the solar incident angle μ_i, i.e., the angle between the direct solar beam and the normal to the surface. These terrain variables are derived from the Shuttle Radar Topography Mission (SRTM, (Farr et al., 2007)) high-resolution (90m) terrain information.

In order to compute the sky view factor, we use the rapid procedure proposed by Dozier and Frew (1990), whereby the unobstructed fraction of sky hemisphere is approximated as

$$V_d \simeq \frac{1}{2\pi} \int_0^{2\pi} \left[cos\theta_s sin^2 H_\phi + sin\theta_s cos\left(\phi - \phi_s\right)\left(H_\phi - sinH_\phi cosH_\phi\right) \right] d\phi \tag{3}$$

for a point with slope θ_s, aspect ϕ_s and horizon angle H_ϕ (i.e., angular distance between zenith and local horizon along the generic azimuth direction ϕ). The terrain configuration, which quantifies the reflected radiation received by surrounding slopes in direct sight, can then be obtained as $C_t \simeq (1 + cos\theta_s)/2 - V_d$ following the approach by (Dozier and Frew, 1990).

While fields of V_d and C_t can be computed offline for any given elevation map, the sun's incidence angle on a surface does depend on the sun's position through the local zenith and azimuth angles (θ_0, ϕ_0)

$$\mu_i/cos\theta_s = cos\theta_0 + \sin\theta_s \tan\theta_0 cos(\phi_s - \phi_0) = \mu_0 + \sin\theta_0\left(S_{sa}\sin\phi_0 + C_{sa}\cos\phi_0\right) \tag{4}$$

where topographic information is encoded in the two terms $S_{sa} = \sin\theta_s \sin\phi_s/cos\theta_s$ and $C_{sa} = \sin\theta_s \cos\phi_s/cos\theta_s$. Here μ_i is the cosine of the solar incidence angle (i.e., angle between the incoming direct light beam and the normal to the land surface) while μ_0 is the cosine of the solar zenith angle (i.e., the incidence angle with respect to a horizontal plane). Additionally, for parameterizing the effect of topography on diffuse radiation we use a standardized elevation $h_n = (h - \mu_h)/\sigma_h$ obtained normalizing elevation based on its grid cell average μ_h and standard deviation σ_h.

For the purpose of parameterizing solar fluxes, we divide these terrain variables by the local terrain slope obtaining the normalized variables $\tilde{\mu}_i = \mu_i/\cos\theta_s$, $\tilde{V}_d = V_d/\cos\theta_s$, and $\tilde{C}_t = C_t/\cos\theta_s$ as recommended by (Lee et al., 2013). Note that while $V_d \in [0, 1]$, the ratio $\tilde{V}_d = V_d/\cos\theta_s$ can sometimes be larger than 1. In previous work (Lee et al., 2011) these terrain predictors are averaged over an area representative of an entire model grid-cell and used as predictors to derive average correction terms f_i for the 5 flux components introduced in Section 2.1. Here, high resolution fields of these predictor variables are first computed based on the original 90m digital elevation maps. These fields are then employed to inform the partitioning of the land domain

into a set of tiles for which we expect topography to have a similar effect on radiation. This step is achieved using a hierarchical clustering methodology described next. Based on this partitioning, relations to predict the topographic effects on radiation (the f_i's) will be applied to each tile independently.

2.4 Hierarchical clustering of terrain properties

In order to capture the spatial variability of radiative fluxes, here we employ a hierarchical multivariate clustering approach (HMC) which was recently introduced to study the role of heterogeneity in hydrological and land models (Chaney et al., 2016, 2018). Here we tailor HMC to the case of shortwave radiative fluxes by performing the land clustering based on terrain properties (namely $\tilde{\mu}_i$, $\tilde{V}_d$, and $\tilde{C}_t$) which are known to modulate the downwelling radiation over mountains as discussed in the previous section.

The land fraction of the study sites, which are chosen to represent in size a typical ESM grid cell, is first divided in a maximum of three components: soil, glacier, lake. The soil fraction is then subdivided into a set of *tiles* characterized by homogeneous terrain properties relevant for capturing the effects of topography on radiative transfer. Additionally, lake and glacier areas, where present, are treated as individual separate tiles. We note that in the domains selected for this study lake and glacier areas constitute a small fraction of the total grid cell area. When applying the methodology to areas where glaciers cover a large fraction of the grid cell, it may be useful to also partition glacier areas in multiple clusters. This can be done following the same methodology described here, since for the purpose of radiation-terrain interactions the only relevant parameters would be the average albedo of each cluster (land or glacier). In our approach, the land clustering is based on 4 terrain variables: The normalized sky view factor, terrain configuration, S_{sa}, and C_{sa}. Note that these variables are independent of the sun's position. Once the direction of the incoming beam is given (ϕ_0 and $\cos\theta_0$), average values of S_{sa} and C_{sa} over any given tile uniquely identify the solar incident angle for each point on the land surface by means of Eq. 4.

A conceptual summary of this clustering procedure is described in Figure 3. The digital elevation map (Figure 3A) is used to compute the drainage network (Figure 3E) necessary to partition the domain in basins (Figure 3B, 3C) based on a threshold area of 1×10^5 m^2. Basins are in turn subdivided in hillslopes (Figure 3F) following Chaney et al. (2018): Each basin is divided in up to three contiguous hillslope elements, corresponding to left side, right side, and headwaters.

Then, hillslope elements are aggregated in k *"characteristic hillslopes"* via k-means clustering (MacQueen et al., 1967) in the 4-dimensional space of the variables $\tilde{V}_d$, $\tilde{C}_t$, S_{sa}, and C_{sa}; this enables to obtain land units characterized by similar radiation-topography interaction. Figure 3G shows the spatial distribution of these characteristic hillslope clusters for the case $k = 5$.

Finally, each of these k land units is further partitioned into p sub-units by a second application of the k-means clustering algorithm based on the 4 variables $\tilde{V}_d$, $\tilde{C}_t$, S_{sa}, and C_{sa}. In figure 3H we show the result of this procedure which yields 25 tiles in this example.

In this application any areas covered by glaciers or lakes are treated as separate land units. Therefore, in the current configuration the number of tiles (n_t) used to describe land heterogeneity within a single land model grid cell vary between $k \cdot p$ and $k \cdot p + 2$ depending on the presence of lake and glacier units. The reason for the first step (subdivision of land in characteristic

hillslopes) originates from the desire of partitioning land in hydrologically coherent units. In the context of shortwave radiation received by land, it is important to understand what is the effect and the benefits of this multilevel clustering. Therefore, we will test the methodology for different tile configurations over the same domains.

A natural test for the ability of the tiled grid of reproducing the actual spatial distribution of solar radiation can be performed as follows: We test here the results for multiple HMC configurations obtained by varying the number of characteristic hillslopes (k) as well as the number of land units within each characteristic hillslope (p). For illustration purposes, we consider two cases: a fixed value of $k = 5$ and a varying p, and the opposite (varying k, setting $p = 5$). This experiment leads to a set of grid configurations with a number of tiles per grid cell varying from 5 to 1000, with different weights given to the first level (partitioning of land in hillslopes) and the second level, in which each characteristic hillslope is further subdivided in p homogeneous land units contributing to the overall number of tiles n_t. This experiment thus elucidates the relative performance of the two different levels of the hierarchical clustering approach in capturing the spatial heterogeneity of the domain.

Therefore, based on this procedure, the land model grid cells are subdivided into a number of tiles n_t. A maximum of two additional tiles can be included representing lake and a glacier areas, if these are present in a given grid cell. Glacier boundaries are determined using the GLIMS database (Raup et al., 2007). Each tile is characterized by statistically homogeneous values of the variables of interest for 3D radiative transfer. Over each tile $t = 1, \ldots, n_t$ we then compute the average value of each predictor variable. For a generic variable $\Theta \in \left\{ \tilde{V}_d, \tilde{C}_t, S_{sa}, C_{sa} \right\}$ we have

$$\langle \Theta \rangle_t = \frac{\sum_{i=1}^{n_p} A_i \Theta_i \mathbb{1}_{t,i}}{\sum_{i=1}^{n_p} A_i \mathbb{1}_{t,i}} \tag{5}$$

with the $< \cdot >_t$ operator representing the operation of average over the points classified as part of tile t, $\mathbb{1}_t$ is the indicator function selecting tile t ($\mathbb{1}_{t,i} = 1$ if pixel i of the high resolution terrain map belongs to tile t, $\mathbb{1}_{t,i} = 0$ otherwise). A_i and Θ_i are area and the value of the property Θ computed for the i-th pixel in a high resolution terrain map with n_p pixels. For the solar incidence angle, once the solar position is known we can write its average value over a tile t as

$$\langle \tilde{\mu}_i \rangle_t = \mu_0 + \sin \theta_0 \left(\langle S_{sa} \rangle_t \sin \phi_0 + \langle C_{sa} \rangle_t \cos \phi_0 \right) \tag{6}$$

Therefore, the average values of these quantities over each tile represent the 'characteristic' value of the properties over that tile and can be used to summarize the effect of multi-scale radiative transfer over mountainous regions.

2.5 A predictive model for the flux correction terms

The final step needed in order to parameterize the effect of complex topography on incident shortwave radiation is specifying a predictive model to link the terrain variables defined in Section 2.3 to the 5 flux components (Sec. 2.1). This step will enable to extend the results of costly ray tracing simulations at the global scale, and provide predictive equations which can be directly applied to high resolution terrain maps as well as to the local averages from the tiling structure defined in Sec. 2.4.

Here we focus on two different approaches, namely a multiple linear regression model (MLR, based on the previous LLH parameterization) and on an alternative approach based on random forest regression (RFR). We explore these two distinct

families of statistical models in order to evaluate the potential role on nonlinearity for different radiation flux terms, keeping in mind that MLR, the simpler statistical model, is in general to be preferred due to the greater ease of interpretation as well as the reduced computational expense when employed in Earth System Models.

270   MC photon tracing simulations are performed at the native 90 m resolution of terrain products available. In the following analysis, results are coarsened at a range of spatial scales up to 10 km in order to test the robustness of the proposed parameterization to the spatial scale of the terrain variable used as predictors, and explore potential dependencies of radiation-topography interaction on the spatial scale considered. In each case, both MC simulation results and terrain properties are averaged at the same spatial resolution in order to train and test the predictive model at that specific spatial scale. MC simulations correspond-

275 ing to the 3D case (i.e., over a three dimensional surface) and over a flat surface (plane parallel case, PP) were subtracted in order to compare the "true" flux deviations as defined in eq. (1). Additionally, given the finite extension of the domain used in the MC simulations, spurious effects may be present due to the periodic boundary conditions imposed, especially for the lower values of solar zenith angle. To mitigate this issue, only the central part of each simulation domain (of size $\sim 1° \times 1°$) is used to train the predictive model; A fraction of size 0.2 times the linear dimension of the domain in discarded at each boundary.

280   The MC simulations were repeated for varying zenith angles (from $\mu_0 = 0.1$ to $\mu_0 = 0.85$) and 4 azimuth angles. The results for each azimuth are pulled together so that a single predictive model for each zenith angle is derived. For application to ESMs, the results should be interpolated when predictions for a generic zenith angle are needed.

After training each model for each solar zenith angle and flux component, we obtain a set of predictive equations linking the f_i's (i.e., the normalized deviation between 3D and PP case) to the terrain predictors at the same spatial scale:

$$285 \quad f_{dir} = g_{dir,m,\cos\theta_0,\Delta x}\left(\langle\tilde{V}_d\rangle_{\Delta x}, \langle\tilde{\mu}_i\rangle_{\Delta x}\right) \tag{7}$$

$$f_{dif} = g_{dif,m,\cos\theta_0,\Delta x}\left(\langle\tilde{V}_d\rangle_{\Delta x}, \langle\tilde{\mu}_i\rangle_{\Delta x}, \langle h_n\rangle_{\Delta x}\right) \tag{8}$$

$$f_{rdir} = g_{rdir,m,\cos\theta_0,\Delta x}\left(\langle\tilde{V}_d\rangle_{\Delta x}, \langle\tilde{C}_t\rangle_{\Delta x}, \langle\tilde{\mu}_i\rangle_{\Delta x}\right) \tag{9}$$

$$f_{rdif} = g_{rdif,m,\cos\theta_0,\Delta x}\left(\langle\tilde{V}_d\rangle_{\Delta x}, \langle\tilde{C}_t\rangle_{\Delta x}\right) \tag{10}$$

$$f_{coup} = g_{coup,m,\cos\theta_0,\Delta x}\left(\langle\tilde{V}_d\rangle_{\Delta x}, \langle\tilde{C}_t\rangle_{\Delta x}, \langle\tilde{\mu}_i\rangle_{\Delta x}\right) \tag{11}$$

290   where g represent the parametric relations linking flux correction terms to terrain variables for different predictive models ($m = MLR$ or $m = RFR$). These equations are derived for each flux component, solar zenith angle $\cos\theta_0$ and spatial scale Δx. We note that these equations were derived for a single surface reflectivity value. The direct and diffuse flux components are independent on albedo; Reflected fluxes are linearly dependent on albedo so that predicted value can be rescaled by the surface albedo. Finally, g_{coup} is nonlinearly dependent on the surface albedo so that predictions for different albedo values

295 can e.g. be obtained by interpolation (Lee et al., 2011). Once the f_i dimensionless predictions are available, the dimensional value of shortwave fluxes over rugged terrain can finally be obtained from Eq. (1). In general, simply applying a correction to the downward radiation received by land will not ensure energy conservation. This is expected in general, as some of the 3D topographic effects parameterized here would lead in general to energy fluxes between neighbouring land model grid cells. A

procedure was proposed by (Lee et al., 2015) which can be used to address this issue. In this approach, an effective albedo α_{3D} is computed for each land grid cell, such that a grid—cell characterized by this α_{3D} and forced by plane-parallel radiation (PP) absorbs the same amount of radiation as in the case of a surface characterized by actual land albedo α, while forced by the 3D-corrected downward radiation fluxes. By returning the 3D albedo (which effectively represents the reflectivity of a "rough" but flat land surface) to the atmosphere, energy is conserved while accounting for the 3D topographic correction.

3 Results and Discussion

3.1 Spatial distribution of solar irradiance

A representative output obtained from Monte Carlo ray tracing simulations for the Eastern Alps domain is portrayed in Figure 4, featuring the spatial distribution of differences between 3D topography and PP case for a given incoming solar beam direction, while fields of the corresponding terrain variables for the same domain are reported in Figure 5.

The direct flux appears prominently modulated by the presence of topography, with the distribution of shaded slopes following that of solar incident angles computed based on the solar angles for the current simulation (Figure 5). In the case of the diffuse flux, differences between the 3D and PP simulations are less apparent, while a similar behavior is observed for the reflected flux components.

From visual inspection of these simulation results, it is apparent that the spatial variation in the direct flux are primarily controlled by the solar incident angle. The diffuse flux, on the other hand, shows a spatial variability primarily consistent with that of the sky view factor, as expected based on previous studies (Chen et al., 2006). Reflected and coupled flux spatial variability appear more complex, potentially controlled by the terrain configuration. This exploratory analysis reveals that, with the sole exception of the direct flux component, variations in downward fluxes are arguably not explained by a single linear relation, but can in general involve multiple terrain predictors and potentially nonlinear effects. This hypothesis will be tested in the next section by examining the skill of a linear and nonlinear model in describing these relationships.

For the direct flux, histograms of the normalized differences between PP and 3D simulations are featured in Figure 6, where the simulation results have been aggregated at a range of increasing spatial averaging scales. For low solar zenith angles, the frequency distribution of f_{dir} tends to have an atom in at -1, lower boundary value corresponding to the case of complete shade. This is clearly a limitation for the linear model approach, since this behaviour imposes a nonlinear relation between f_{dir} and terrain variables (solar incident angle and sky view). However, averaging the results at increasing spatial scales we see this effect progressively diminishes, as the probability of a complete shade decreases. For both the domains examined in Figure 6, this behavior is similar and similarly decreases with the cosine of the solar zenith angle. We note that at spatial scales larger than approximately $5 \ km$ the effect disappears. We note that it is a this range of scales that previous parameterization of 3D radiation over mountains were trained (Lee et al., 2011).

3.2 Model evaluation: sensitivity to the spatial scale and role of nonlinear effects

330 To quantify the sensitivity of the proposed methodology on the resolution of terrain data, we aggregate the MC-simulated radiation fields and corresponding terrain variables fields at increasing spatial scales ($L_s \in \{0.5, 1, 2, 3, 5, 10\}$ km) and in each case fit the predictive models as described in Sec. 2.5, comparing the relative performance of multiple linear regressor and random forest predictions.

As shown in Figure 7, the difference between RFR and MLR prediction skills is most relevant for the direct and direct-
335 reflected flux components in the case of low solar zenith angles, and are also significant in the case of diffuse and coupled fluxes. In these two latter cases, the difference between RFR and MLR skills persist for all μ_0 values and thus is not limited to cases where the sun is relatively low on the horizon, as is the case for direct and direct-reflected fluxes. The reflected-diffuse component is quite linear, as shown by the small difference between random forest and linear regressors predictive skills. For the direct-reflected flux this only happens for large enough values of the cosine of the solar zenith angle ($\mu_0 > 0.55$).

340 The predictive model for the direct flux shows high values of coefficients of determination (R^2), with similar performance for RFR and MLR, indicating that a linear model is well suited to describe this quantity. The only discrepancy is observed for very low solar angles ($\mu_0 = 0.1$), a case in which RFR outperforms the MLR. We believe this is primarily due to the effect of completely shaded areas in the domain, which are characterized by sharp transitions better described by ensemble of decision tree due to the nonlinear behavior. We note that this effect is relevant only for comparatively small spatial scales ($L_s < 3$ km)
345 and low solar angles, and similarly impacts the direct-reflected flux, which as expected is modulated by the amount of direct light received at the surface. In the case of larger spatial averaging scales and larger solar angles, the MLR describes the direct flux with great accuracy. Moreover, the poorer model performance at the low solar angles is mitigated by the fact that these conditions (e.g., dusk and down) generally account for a small fraction of the irradiance received by land over most geographic locations and times of the year.

350 Reflected-direct and Reflected-diffuse fluxes also exhibit a clear linear dependence on the terrain predictors, with MLR and RFR having similar R^2 values at all averaging scales and solar angles, with the only difference between the two approaches again appearing for the reflected-direct flux for very small solar angles.

Appreciable differences between MLR and RFR are observed for diffuse and coupled fluxes. In these cases, it appears that diffuse radiation is better described by a nonlinear model, as is the case for irradiance originating from multiple reflections
355 at the ground and atmospheric scattering (f_{coup}). In these cases, consistent with previous findings by (Lee et al., 2011), the predictive ability of linear models is lower.

These out-of-sample results were obtained using training data from the Peru domain and testing data from the EastAlps domain. For completeness, we did also run the opposite configuration (switching training and testing domains) finding similar results.

360 In all cases in which predictive skills of MLR and RFR diverge, we observe that when comparing in-sample and out-of-sample performance the loss of predictive skill is larger in the case of RFR. This finding is not surprising. Given the additional model complexity of the RFR approach with respect to MLR, our analysis confirms that it is more prone to overfitting the

calibration dataset. Once this overfitting tendency is accounted for, our analysis selects the MLR as model of choice since applications of the methodology do inevitably require extrapolation of the results to new domains.

365   Based on these results, we generally recommend the adoption of the linear regression models at least for direct and reflected fluxes, given the good performance and model simplicity. Applications of RFR are in principle possible in ESMs and has been shown here to have good predictive performance for this specific problem. However, this comes at the cost of a lower interpretability and based on the present analysis here RFR is not the model of choice, given the limited increase in predictive skill with respect to MLR especially when tested in cross validation.

370   ### 3.3   Nonlinearity and effect of averaging for the direct flux

The direct flux component is characterized by a nonlinear behavior in the case of completely shaded areas.

This behavior should be taken into account in our model, as averaging terrain properties over tiles with varying characteristic size and spatial configuration would lead in general to changes in the average predicted f_{dir} for a given tile if model predictions are averaged over areas which, in the high resolution true field, include partial shades. One possible way to capture this behavior

375   is to predict f_{dir} first over an entire grid cell to obtain its average value, and then impose that tile-by-tile predictions must match the average value of the direct flux correction over the entire grid cell ($\langle \tilde{f}_{dir} \rangle$). This can be achieved through the following transformation for a generic tile $i = 1, ... n_t$. We define the corrected value $f_{dir}^{(i)}$ as

$$\tilde{f}_{dir}^{(i)} = \langle f_{dir} \rangle + \left(\langle \tilde{f}_{dir} \rangle - \tilde{f}_{dir}^{(min)} \right) \frac{f_{dir}^{(i)} - \langle f_{dir} \rangle}{\langle f_{dir} \rangle - f_{dir}^{(min)}} \tag{12}$$

This correction was obtained by imposing that the $\tilde{f}_{dir}$ values predicted by the model for each tile conserve the grid cell

380   average value, by correcting the original value $\langle f_{dir} \rangle = \sum_{i=1}^{n_t} p_i f_{dir}^{(i)}$, with p_i the fractional area of the grid cell assigned to tile i. This transformation also preserves the minimum value over the grid cells, so that $\tilde{f}_{dir}^{(min)} = f_{dir}^{(min)} = min_{i=1}^{n_t} f_{dir}^{(i)}$. For other flux variable this correction is not necessary if a linear model is used for predicting their average values over tiles, as done here.

Figure 8 shows the frequency distribution of corrections for the various flux terms varying the number of tiles. In particular, for the direct flux, the distribution of tile-by-tile estimates is shown to converge to the histograms of full high resolution results

385   for $n_t = 250$ tiles. Thus, application of the correction given in eq. (12) allows to preserve the grid cell average correction while adequately representing the sub-grid scale variability of f_{dir}.

3.4   Model sensitivity to the number of tiles used

The predictive model can be used to produce tile-by-tile estimate of flux differences and compare results with those predicted for the original high resolution terrain map. We repeat this analysis for different configurations of the hierarchical clustering

390   scheme, so as to test the sensitivity of the results to the number of tiles used to characterize domain heterogeneity. While the MC simulations were performed over two domains only, here we perform the clustering analysis over all three domains comparing predictions obtained by applying the 3D radiation corrections to the original high-resolution terrain data with the same approach to the sub–grid tiling structures for a varying number of land clusters. We expect a larger number of tiles to lead

to a better representation of the flux component over rugged terrain. However, a too large number of tiles would not be feasible
for running ESMs over large domains or the entire globe.

An example of the spatial distribution of tiles obtained by applying the HMC algorithm is reported in Figure 9 for the
EastAlps domain, where the land domain is partitioned into 5 and 25 clusters, respectively. Two additional tiles are used to
represent lakes and glaciers, which are present over this domain, albeit accounting for a small fraction of the surface. Once the
tiled grid is defined using the HMC method, local averages of terrain parameters can be computed directly over each land unit.
For example, the lower panels in Figure 9 show the spatial distributions of the terrain view factor $\tilde{C}_t$) averaged over each tile,
showing that larger number of tiles greatly improve the representation of the spatial variability of topography.

We then tested the ability of the tiled grid of reproducing the actual spatial distribution of solar radiation by examining first
the results obtained by varying separately the number of characteristic hillslopes k (while keeping p fixed) and comparing then
with the results for variable p and constant k. This analysis is intended to test the robustness of the method to different sub–grid
land partitioning schemes.

Figures 10 and 11 show how increasing the number of land tiles improves the description of the direct flux and diffuse
flux components, respectively, over the EastAlps domain. Note that the same disaggregation of the domain in tiles is used for
predicting the distribution of both variables. Even in the case of a fairly low number of tiles (e.g., 5 tiles in panels 10B and 11B)
the sub–grid structure is able to capture the main feature of both direct and diffuse radiation fields, even though their variations
are known to be controlled by different terrain properties (primarily aspect and sky view, respectively, as can be seen by the
spatial distribution of direct and diffuse fluxes in the high resolution results). For both f_{dir} and f_{dif}, the tile-by-tile predictions
appear to converge to the original high resolution field when increasing the number of tiles (results for 25 and 250 tiles are
shown in lower panels of Figures 10 and 11). Note that this result is quite significant, since for the domain examined here the
number of points need to obtain the high resolution field without using a clustering approach would be of the order of 10^6 (for
a $1° \times 1°$ grid cell at the native 90m resolution of SRTM data).

To obtain a more quantitative description of the convergence to the high-resolution fields, we show how spatial statistics of
the radiation fields (spatial standards deviation σ_x, skewness γ_x and kurtosis ξ_x) vary with increasing tile count with respect to
the same statistics computed for the reference high resolution field.

For all the terrain predictors (Figure 12) we find that increasing the number of tiles, the spatial variability of terrain predictors
converges to that of original high-resolution fields, as expected. However, this convergence appears to be faster for the solar
incidence angle when compared to $\tilde{V}_d$ and $\tilde{C}_t$. Higher order statistics of the spatial fields (skewness and kurtosis) also tend
to converge to the high resolution field values, although with a larger variability. While spatial standard deviation is generally
used as a metric for assessing spatial variability, examining skewness and kurtosis helps to make sure the entire distribution
of tile-by-tile results is converges to the high resolution benchmark, since they better capture asymmetry and extremes in tile
values. However, we note that these metrics are not very meaningful for the smallest number of tiles shown in Figure 12) due to
the small sample size. However, the fact that for a large enough number of tiles (e.g., $n_t > 20$) these metric appear to converge
to the true values increase our confidence that the hierarchical clustering scheme provides a good description of the topography
heterogeneity.

For the flux variables (Figure 13) we find a similar behavior, with convergence of the spatial standard deviation being generally faster that that higher order statistics. In this case, the convergence is faster for the direct flux while slower for all other flux component, as expected since F_{dir} is primarily controlled by $\tilde{\mu}_i$ while the other flux components are show relevant dependence on either sky view factor or terrain configurations.

To further analyze the configuration of the tiling structure used, we also tested different tiling configurations obtained by fixing the number of characteristic hillslopes ($k = 5$) and varying the number of lower-level land units in each hillslope (p), or conversely varying k with $p = 5$ fixed. Results from both these approaches are reported in Figures 12 and 13. We find that generally convergence is faster using a larger p, i.e., dividing each characteristic slope in a larger number of tiles as opposed to increasing the number of characteristic hillslopes. This is not surprising. However, differences are generally small, and therefore the model proposed appears flexible and can in principle be applied with tiling predefined in order to accommodate for other physical processes as well.

3.5 Magnitude of predicted fluxes over varying atmospheric conditions

The presence of clouds adds considerable complexity to the problem of radiation-topography interactions, and has not been considered in our work. A complete understanding of 3D land - atmosphere interactions would require to extend our analysis to a large range of atmospheric conditions, which would be computationally costly requiring a large number of ray tracing simulations, and would arguably lead to a more complex parameterization requiring a larger number of parameters to estimate 3D topographic radiation corrections. Previous work such as (Lee et al., 2011) also focused on clear sky conditions. Although obtained assuming fixed atmospheric properties, the 3D-terrain corrections for radiation fluxes have been formulated in dimensionless form (Eq. (1)) so that they can be applied as a first order correction to radiation received by land over varying atmospheric conditions. In different atmospheric conditions (clear vs. cloudy sky), the relative magnitude of the 5 radiation flux components can vary substantially. To show the magnitude of these changes, we compute here the magnitude of the flux 3D effects in dimensional form for the case of "clear sky" (i.e., aerosols but not clouds) and "total sky", i.e., atmospheric column with cloud cover and aerosol. These computations were made using the Fu-Liou radiative transfer scheme (Fu and Liou, 1992) using a standard mid latitude summer atmospheric profile.

Results for clear sky conditions and are shown in Figure 14 and Figure 15, while the case of cloudy sky is shown in Figure 16. While the overall downward flux is smaller in the case of cloudy sky, the direct and reflected-direct fluxes are zero so that the entire downward flux is comprised of diffuse, reflected-diffuse and coupled components. For the coupled flux, the spatial variations are similar in the two cases, with the most frequent values in the range -2 to $8\,\mathrm{Wm}^{-2}$. For diffuse fluxes the clear sky case is characterized by larger magnitude of 3D topographic effects, and this difference is even more marked in the case of reflected-diffuse fluxes.

3.6 Compatibility with existing sub – grid tiling schemes

The approach proposed in our manuscript to design a sub–grid structure was developed keeping in mind the necessity of describing not only radiation, but also other physical processes at the sub—grid scale. The GFDL model, as several current

generation ESMs, resolves each sub-grid tile as a single 'column' coupled with the atmosphere. Therefore, these tiles should be flexible enough to meet the contraints posed by different physical processes. In our case, a single–level terrain clustering would suffice for the purpose of parameterizing 3D radiation-topography interactions. However, the multi-level clustering used here

465 accounts is flexible enough to accomodate multiple physical processes. For example, the outer level clustering (i.e., the partition of the domain in k characteristic hillslopes) is designed to obtain hydrologically coherent units, so that processes like runoff and groundwater flow can be resolved in each homogeneous land unit (Chaney et al., 2018). Here we include this flexible sub—grid structure, and in our sensitivity study (Figure 13) we compare different specifications of k and p (number of characteristic hillslopes, and number of inner clusters within each hillslope) to test the sensitivity of our parameterization to these changes

470 in sub-grid structure, finding that our results are robust to the specific tile structure selected. Finally, it is possible that other variables may need to be added to the clustering to account for sub—grid heterogeneity of other processes. For example, land use or soil properties. This can be directly done with the framework used here, at the price of an increase in the number of tiles used. Producing an effective global–scale model grid able to meet these demands is possible but requires inevitable trade-offs. The analysis in this paper contribute to this effort by quantifying the number of tiles needed over mountainous terrain

475 for the sole purpose of capturing the spatial variability in shortwave radiation. We note that in the case of the GFDL ESM, the model infrastructure is already suited for grids of this type, which can be characterized by an uneven number of sub–grid units in different grid cells depending on the local terrain properties. On the model start, the land grid cells can be distributed among available processors based on the estimated workload needed for each of the cells, assuming that computational cost is proportional to the number of sub–grid units. Therefore, the work per processor is roughly the same, and the imbalance

480 resulting from this uneven grid structure is minimized.

3.7 Comparison with grid cell-average correction

The parameterization developed here can in principle be applied both to high resolution terrain partitioned in tiles and to the original grid cell area. However, our analysis of the model goodness of fit (Figure 7) shows that the predictive models at different spatial resolutions (i.e., spatial averaging scale) show varying performance, which increases with spatial scale.

485 Therefore, according to this analysis, the model predictions for 3D effects over an entire grid cell have the best performance. However, this comes at the cost of losing information about the sub—grid scales. Based on these considerations, it would be desirable to have a model with the best accuracy over an entire grid cell, that is at the same time able to describe tile-by-tile spatial variations in radiation fluxes received at the surface. In order for this to be possible, the parameterization developed here should be able to yield the same results when i) applied to each tile separately and then averaged over the grid cell,

490 and ii) applied to the grid average terrain predictors. We found that the parameterizations proposed here have this property for 4 flux components (diffuse, coupled and reflected fluxes) but not for the direct flux. This is because the behavior of the parameterization in the case of complete shade areas (for which f_{dir} assumes the lower bound value -1) is not constant across averaging scales due to the varying area of hill shades. We show this behavior in Figure 17, where once averaged over an entire grid cell, the results of the tile-by-tile parameterization for the direct flux appears to overestimate the grid-cell average

495 3D topographic effect with respect to the grid cell average estimate of f_{dir}. This discrepancy can be resolved by the use of Eq.

(12) which, once applied to the direct flux, allows to impose the tile-by-tile correction to match the grid cell average correction. Result of this correction is shown in Figure 17. Therefore, once this correction is employed for the direct flux, this approach can at the same time conserve the area average effect while providing information about the sub–grid variability of the radiative fluxes.

3.8 Discussion on the dependence on albedo and its spatial variability

The methodology described here has been developed for a surface with a uniform and fixed albedo value. For applying the methodology to an ESM, the radiation corrections which are albedo - dependent (reflected and coupled fluxes) should be evaluated for the specific surface albedo value as discussed in Section 2.5. However, in the presence of surfaces with spatially varying reflectivity, it is inevitable that different land tiles in the same grid cell will be characterized by different albedo values. For example, this can happen in the case of partial snow cover, or in the case of different vegetation types along a gradient in elevation. While here the 3D radiation correction is applied to each tile independently, it is expected that reflected and coupled fluxes should include contributions from nearby tiles characterized by different albedo values. At present our methodology does not address explicitly these interactions between tiles with different albedo. We note here two main difficulties in constructing such a model: First, its validation would require an extensive set of costly MC simulations to train the model over surfaces with varying reflectivity. Second, explicitly accounting for the reflectivity of nearby slopes may require a more complex statistical model, and it would not be easy task given the complex geometry of the tile structure adopted in our work. Solving these two important challenges should be object of future research.

4 Conclusions

Here we described a methodology to compute solar fluxes over mountainous terrain, accounting for the sub–grid variability of topographic properties within a characteristic ESM grid cell. Topographic parameters modulating the incident solar irradiance, combined to results from Monte Carlo radiation simulation over 3D surface, were used to train a predictive model and cluster land surface based on topography-radiation interactions. The methodology as presented here is tailored to a tiling structure scheme recently introduced in the GFDL land model LM4.1 to describe the heterogeneity of hydrological properties. However, we believe this approach can be suitable for applications to others land surface models, as the clustering technique used here allows for a parsimonious description of the spatially varying solar fluxes. For this reason, we tested the sensitivity of the approach to the number of tiles used over independent sites characterized by complex topography. The results appear consistent over different geographical domains, and indicate that even a limited number of tiles can reproduce a significant fraction of the spatial variability observed in the high resolution fields. This result is particularly relevant when compared with standard approaches focused on increasing the land model resolution without adopting a clustering-based approach to construct a sub–grid land structure. Increasing the number of tiles does not only improve the representation of spatial variances, but also improves convergence of higher order statistics. However, even when using a lower number of tiles, the results remain consistent with previously (i.e., the methodology can ensure that the grid cell average correction is downward radiation is

conserved) developed grid-cell average correction and thus are to be considered an improvement with respect to current plane-parallel radiative transfer. Here we found that even a limited number of tiles ($n_t = 10$) recovers a large fraction ($> 60\%$) of the spatial variance of irradiance over high mountain domains. However, we find that a larger number of sub–grid units (of the order of $n_t = 100$) would lead to a further significant improvement. Further increasing the number of tiles above $n_t = 100$ would lead to more modest improvements at the price of a much larger number of tiles required, as shown by the convergence analysis. Therefore, an optimal number of tiles could be between 10 and 100. Using such a large number of tiles in a global model would be ambitious to date, due to its computational cost. However, we note that a global grid can be constructed by coarsening the sub–grid tile structure in area with little or no topography, and using more tiles in areas of complex terrain. Following this approach, constructing a global grid with a global average number of tiles between 5 and 20 (over land $1° \times 1°$ degrees grid cells) is certainly in reach.

The current methodology, as well as previous studies on the topic (e.g., (Chen et al., 2006; Lee et al., 2011)) employed Monte Carlo simulations based on clear sky conditions. Studying the effects of aerosols and cloud in the radiative transfer over complex terrain remains an open research avenue. In particular, the presence of a spatially varying cloud cover could profoundly influence the spatial distribution of irradiance over mountainous terrain. However, in addition to the numerical challenges connected to the radiative transfer problem, including a spatially varying cloud cover would inevitably increase the number of parameters needed to parameterize the radiation received by the surface, thus posing a relevant parameterization challenge.

Studying the relationship between terrain predictors and irradiance differences between 3D and PP cases allowed to quantify the importance of nonlinear effects and the relative skill of linear models and random forest predictors in capturing these relationships. We found that nonlinear effects are relevant primarily at the finer spatial scales, and decrease drastically with spatial averages at increasing spatial scales. This results is consistent with previous investigations at coarser spatial scales based on linear models.

Based on our simulation study over a set mountainous domains, we quantified the difference in downward fluxes originating from topographic effect with respect with that obtained from traditional plane-parallel radiative transfer schemes for varying number of sub–grid tiles. Our results support the implementation of this methodology in the GFDL ESMs, which will be pursued as the next step to evaluate the effects of this correction of water and energy fluxes at the surface.

Code and data availability. The code used in this projects are made available during the review process in a zenodo repository with DOI https://zenodo.org/record/7714735#.ZAvnLLTMIpN.

The preprocessing software used to construct the land database for the GFDL land model v4.1 is included as supplementary material in the zenodo repository https://zenodo.org/record/7720281#.ZAvnArTMIpN. A Model dataset necessary to run the analysis is available in a zenodo repository with DOI https://zenodo.org/record/6975857#.Y8x0kxNByO0

Author contributions. All authors contributed to research design. E.Z. developed software, performed the simulations study, and drafted a first version of this manuscript. All authors contributed to the manuscript.

Competing interests. The authors declare no competing interests

Acknowledgements. The authors acknowledge funding from the NOAA Climate Program Office (CPO) grant number NA18OAR4320123 "3D-Land Energy and Moisture Exchanges: Harnessing High Resolution Terrestrial Information to Refine Atmosphere-to-Land interactions in Earth System Models". Funding support for this work was also provided through Interagency Agreement Number 80HQTR21T0015 from NASA Earth Science Division's High Mountain Asia program. Dr. Lucas Harris and Dr. Linjiong Zhou are acknowledged for their comments and suggestions on an internal review of the manuscript.

References

Bales, R. C., Molotch, N. P., Painter, T. H., Dettinger, M. D., Rice, R., and Dozier, J.: Mountain hydrology of the western United States, Water Resources Research, 42, 2006.

570   Brutsaert, W.: Evaporation into the atmosphere: theory, history and applications, vol. 1, Springer Science & Business Media, 2013.

Chaney, N. W., Metcalfe, P., and Wood, E. F.: HydroBlocks: a field-scale resolving land surface model for application over continental extents, Hydrological Processes, 30, 3543–3559, 2016.

Chaney, N. W., Van Huijgevoort, M. H., Shevliakova, E., Malyshev, S., Milly, P. C., Gauthier, P. P., and Sulman, B. N.: Harnessing big data to rethink land heterogeneity in Earth system models, Hydrology and Earth System Sciences, 22, 3311, 2018.

575   Chen, Y., Hall, A., and Liou, K.: Application of three-dimensional solar radiative transfer to mountains, Journal of Geophysical Research: Atmospheres, 111, 2006.

Dozier, J.: A clear-sky spectral solar radiation model for snow-covered mountainous terrain, Water Resources Research, 16, 709–718, 1980.

Dozier, J. and Frew, J.: Rapid calculation of terrain parameters for radiation modeling from digital elevation data, IEEE Transactions on Geoscience and Remote Sensing, 28, 963–969, 1990.

580   Dubayah, R., Dozier, J., and Davis, F. W.: Topographic distribution of clear-sky radiation over the Konza Prairie, Kansas, Water Resources Research, 26, 679–690, 1990.

Duguay, C. R.: Radiation modeling in mountainous terrain review and status, Mountain research and development, pp. 339–357, 1993.

Dunne, J., Horowitz, L., Adcroft, A., Ginoux, P., Held, I., John, J., Krasting, J., Malyshev, S., Naik, V., Paulot, F., et al.: The GFDL Earth System Model version 4.1 (GFDL-ESM 4.1): Overall coupled model description and simulation characteristics, Journal of Advances in
585   Modeling Earth Systems, 12, e2019MS002 015, 2020.

Essery, R. and Marks, D.: Scaling and parametrization of clear-sky solar radiation over complex topography, Journal of Geophysical Research: Atmospheres, 112, 2007.

Farr, T. G., Rosen, P. A., Caro, E., Crippen, R., Duren, R., Hensley, S., Kobrick, M., Paller, M., Rodriguez, E., Roth, L., et al.: The shuttle radar topography mission, Reviews of geophysics, 45, 2007.

590   Fu, Q. and Liou, K.: On the correlated k-distribution method for radiative transfer in nonhomogeneous atmospheres, Journal of Atmospheric Sciences, 49, 2139–2156, 1992.

Granger, J. and Schulze, R.: Incoming solar radiation patterns and vegetation response: examples from the Natal Drakensberg, Vegetatio, 35, 47–54, 1977.

Gu, L., Baldocchi, D., Verma, S. B., Black, T., Vesala, T., Falge, E. M., and Dowty, P. R.: Advantages of diffuse radiation for terrestrial
595   ecosystem productivity, Journal of Geophysical Research: Atmospheres, 107, ACL–2, 2002.

Gu, Y., Liou, K., Lee, W.-L., and Leung, L.: Simulating 3-D radiative transfer effects over the Sierra Nevada Mountains using WRF, Atmospheric Chemistry and Physics, 12, 9965, 2012.

Hao, D., Bisht, G., Gu, Y., Lee, W.-L., Liou, K.-N., and Leung, L. R.: A Parameterization of Sub-grid Topographical Effects on Solar Radiation in the E3SM Land Model (Version 1.0): Implementation and Evaluation Over the Tibetan Plateau, Geoscientific Model Development
600   Discussions, pp. 1–23, 2021.

Hay, J. E. and McKay, D. C.: Estimating solar irradiance on inclined surfaces: a review and assessment of methodologies, International Journal of Solar Energy, 3, 203–240, 1985.

Helbig, N., Löwe, H., and Lehning, M.: Radiosity approach for the shortwave surface radiation balance in complex terrain, Journal of the Atmospheric Sciences, 66, 2900–2912, 2009.

605   Isard, S.: Evaluation of models for predicting insolation on slopes within the Colorado alpine tundra, Solar Energy, 36, 559–564, 1986.

Lamare, M., Dumont, M., Picard, G., Larue, F., Tuzet, F., Delcourt, C., and Arnaud, L.: Simulating optical top-of-atmosphere radiance satellite images over snow-covered rugged terrain, The Cryosphere, 14, 3995–4020, 2020.

Larue, F., Picard, G., Arnaud, L., Ollivier, I., Delcourt, C., Lamare, M., Tuzet, F., Revuelto, J., and Dumont, M.: Snow albedo sensitivity to macroscopic surface roughness using a new ray-tracing model, The Cryosphere, 14, 1651–1672, 2020.

610   Lee, W.-L., Liou, K., and Hall, A.: Parameterization of solar fluxes over mountain surfaces for application to climate models, Journal of Geophysical Research: Atmospheres, 116, 2011.

Lee, W.-L., Liou, K., and Wang, C.-c.: Impact of 3-D topography on surface radiation budget over the Tibetan Plateau, Theoretical and applied climatology, 113, 95–103, 2013.

Lee, W.-L., Gu, Y., Liou, K., Leung, L., and Hsu, H.-H.: A global model simulation for 3-D radiative transfer impact on surface hydrology

615   over the Sierra Nevada and Rocky Mountains., Atmospheric Chemistry and Physics, 15, 2015.

Lee, W.-L., Liou, K.-N., Wang, C.-c., Gu, Y., Hsu, H.-H., and Li, J.-L. F.: Impact of 3-D Radiation-Topography Interactions on Surface Temperature and Energy Budget Over the Tibetan Plateau in Winter, Journal of Geophysical Research: Atmospheres, 124, 1537–1549, 2019.

Lenot, X., Achard, V., and Poutier, L.: SIERRA: A new approach to atmospheric and topographic corrections for hyperspectral imagery,

620   Remote Sensing of Environment, 113, 1664–1677, 2009.

Liou, K., Lee, W.-L., and Hall, A.: Radiative transfer in mountains: Application to the Tibetan Plateau, Geophysical Research Letters, 34, 2007.

Liou, K.-N.: An introduction to atmospheric radiation, Elsevier, 2002.

MacQueen, J. et al.: Some methods for classification and analysis of multivariate observations, in: Proceedings of the fifth Berkeley sympo-

625   sium on mathematical statistics and probability, vol. 1, pp. 281–297, Oakland, CA, USA, 1967.

Mayer, B.: Radiative transfer in the cloudy atmosphere, in: EPJ Web of Conferences, vol. 1, pp. 75–99, EDP Sciences, 2009.

Mayer, B., Hoch, S., and Whiteman, C.: Validating the MYSTIC three-dimensional radiative transfer model with observations from the complex topography of Arizona's Meteor Crater, Atmospheric Chemistry and Physics, 10, 8685–8696, 2010.

McCabe, G. J. and Clark, M. P.: Trends and variability in snowmelt runoff in the western United States, Journal of Hydrometeorology, 6,

630   476–482, 2005.

Miesch, C., Briottet, X., Kerr, Y. H., and Cabot, F.: Monte Carlo approach for solving the radiative transfer equation over mountainous and heterogeneous areas, Applied Optics, 38, 7419–7430, 1999.

Milly, P. C., Malyshev, S. L., Shevliakova, E., Dunne, K. A., Findell, K. L., Gleeson, T., Liang, Z., Phillipps, P., Stouffer, R. J., and Swenson, S.: An enhanced model of land water and energy for global hydrologic and earth-system studies, Journal of Hydrometeorology, 15,

635   1739–1761, 2014.

Picard, G., Dumont, M., Lamare, M., Tuzet, F., Larue, F., Pirazzini, R., and Arnaud, L.: Spectral albedo measurements over snow-covered slopes: theory and slope effect corrections, The Cryosphere, 14, 1497–1517, 2020.

Pincus, R., Mlawer, E. J., and Delamere, J. S.: Balancing accuracy, efficiency, and flexibility in radiation calculations for dynamical models, Journal of Advances in Modeling Earth Systems, 11, 3074–3089, 2019.

640 Raup, B., Racoviteanu, A., Khalsa, S. J. S., Helm, C., Armstrong, R., and Arnaud, Y.: The GLIMS geospatial glacier database: a new tool for studying glacier change, Global and Planetary Change, 56, 101–110, 2007.

Shevliakova, E., Pacala, S. W., Malyshev, S., Hurtt, G. C., Milly, P., Caspersen, J. P., Sentman, L. T., Fisk, J. P., Wirth, C., and Crevoisier, C.: Carbon cycling under 300 years of land use change: Importance of the secondary vegetation sink, Global Biogeochemical Cycles, 23, 2009.

645 Sirguey, P.: Simple correction of multiple reflection effects in rugged terrain, International Journal of Remote Sensing, 30, 1075–1081, 2009.

Sirguey, P., Mathieu, R., and Arnaud, Y.: Subpixel monitoring of the seasonal snow cover with MODIS at 250 m spatial resolution in the Southern Alps of New Zealand: Methodology and accuracy assessment, Remote Sensing of Environment, 113, 160–181, 2009.

Tesfa, T. K. and Leung, L.-Y. R.: Exploring new topography-based subgrid spatial structures for improving land surface modeling, Geoscientific Model Development, 10, 873–888, 2017.

650 Villefranque, N., Fournier, R., Couvreux, F., Blanco, S., Cornet, C., Eymet, V., Forest, V., and Tregan, J.-M.: A Path-Tracing Monte Carlo Library for 3-D Radiative Transfer in Highly Resolved Cloudy Atmospheres, Journal of Advances in Modeling Earth Systems, 11, 2449–2473, 2019.

Zhao, M., Golaz, J.-C., Held, I., Guo, H., Balaji, V., Benson, R., Chen, J.-H., Chen, X., Donner, L., Dunne, J., et al.: The GFDL global atmosphere and land model AM4. 0/LM4. 0: 2. Model description, sensitivity studies, and tuning strategies, Journal of Advances in
655 Modeling Earth Systems, 10, 735–769, 2018.
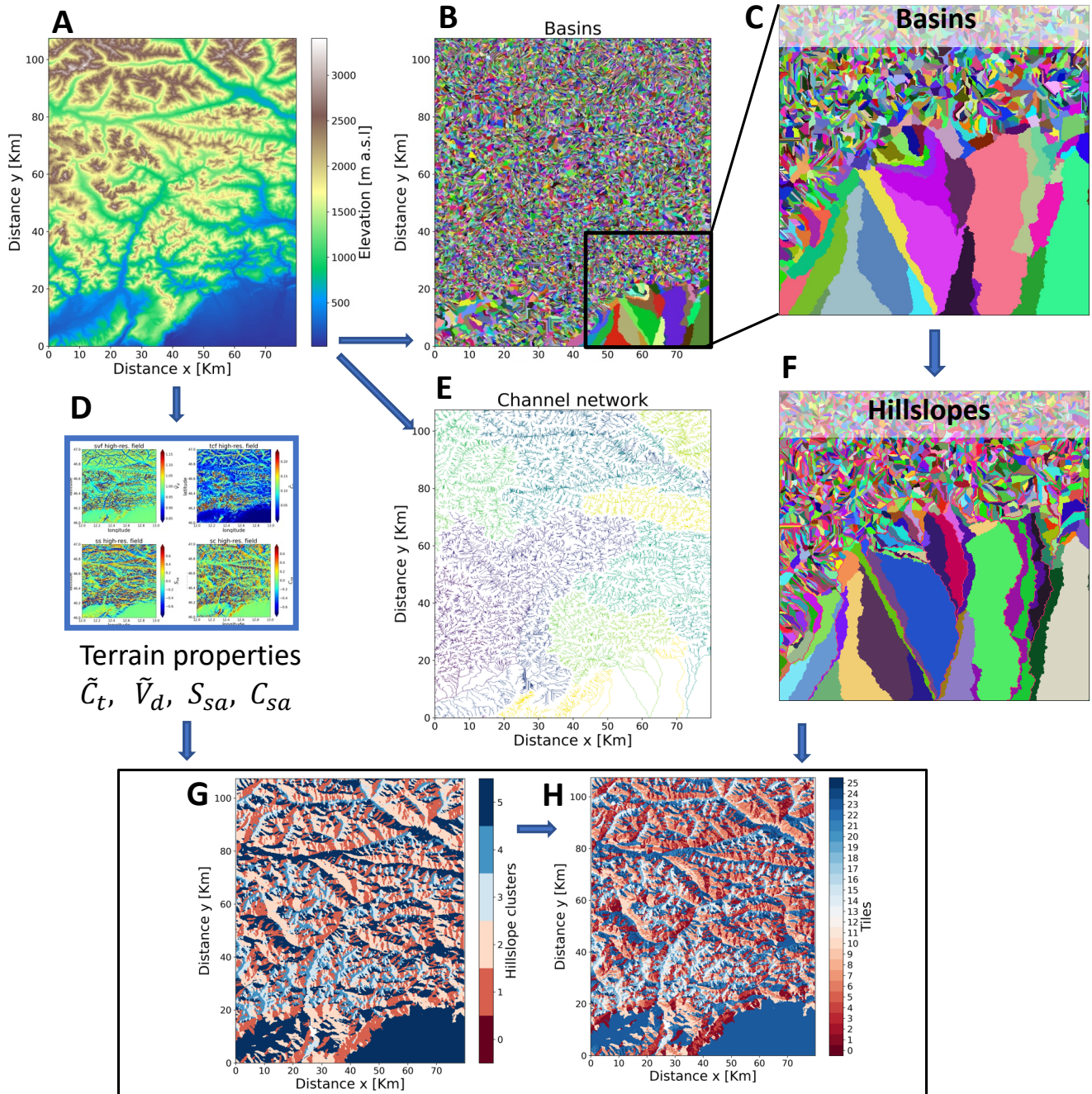
Figure 3. Schematic representation of the land clustering workflow. The land elevation map (A) is used to compute the variables of interest (sky and terrain view factors, and functions of terrain slope and aspect, panel D) which are then used in the hierarchical clustering steps, yielding a map of homogeneous land units needed to parameterize radiation-topography interactions. The delineation of channel network (E), watersheds (B,C) and hillslopes (F) follows the approach developed by (Chaney et al., 2018). The resulting spatial distribution of hillslope clusters and land tiles (corresponding to the two stages of land clustering) are shown in panels (G) and (H) respectively.
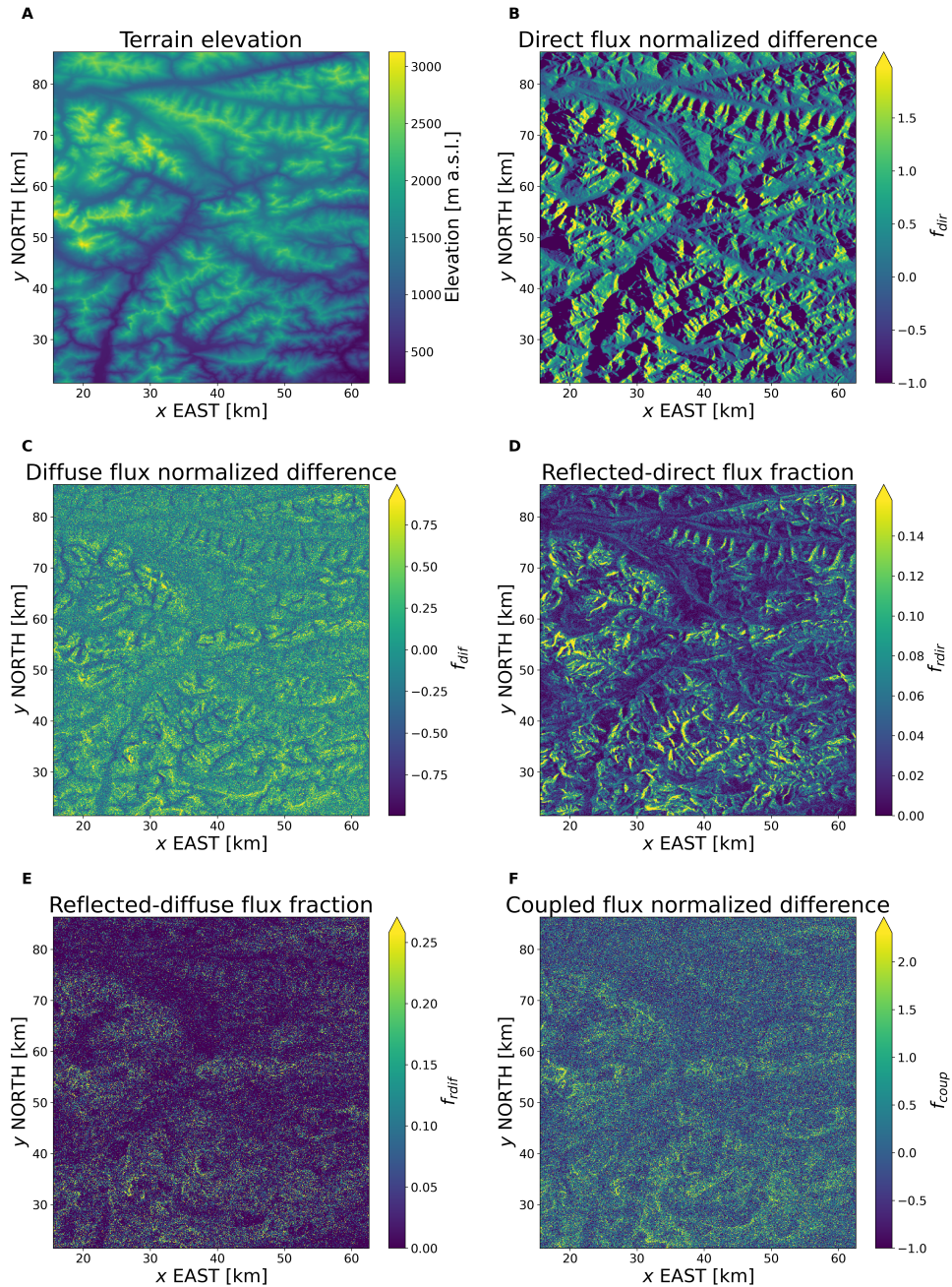
Figure 4. Normalized differences in downward fluxes obtained running Monte Carlo simulations using the real topography and a flat domain, respectively ($\mu_0 = 0.40$, $\phi_0 = \pi/2$). Maps are shown using an equal-area Mollweide projection.
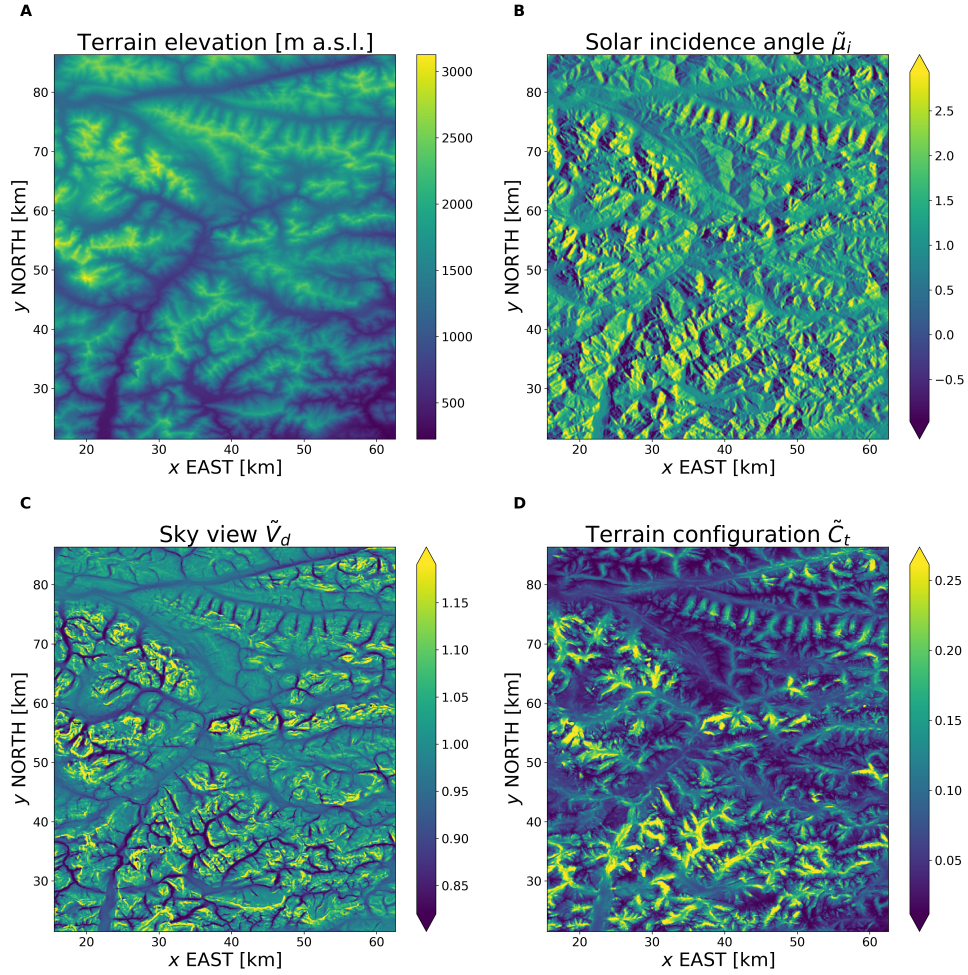
Figure 5. Terrain variables computed for the same domain shown in the previous figure (EastAlps). Solar incidence angle was computed for $\mu_0 = 0.40$, $\phi_0 = \pi/2$. Maps are shown using an equal-area Mollweide projection.
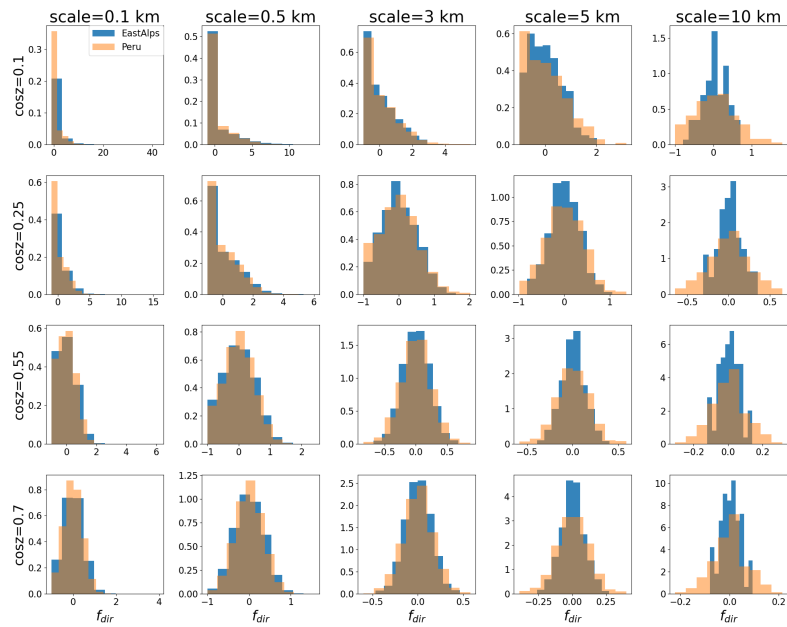
Figure 6. Histograms of the direct radiation correction f_{dir} between the 3D and PP cases, for varying zenith angle and spatial averaging scale, for the Peru and EastAlps domain.
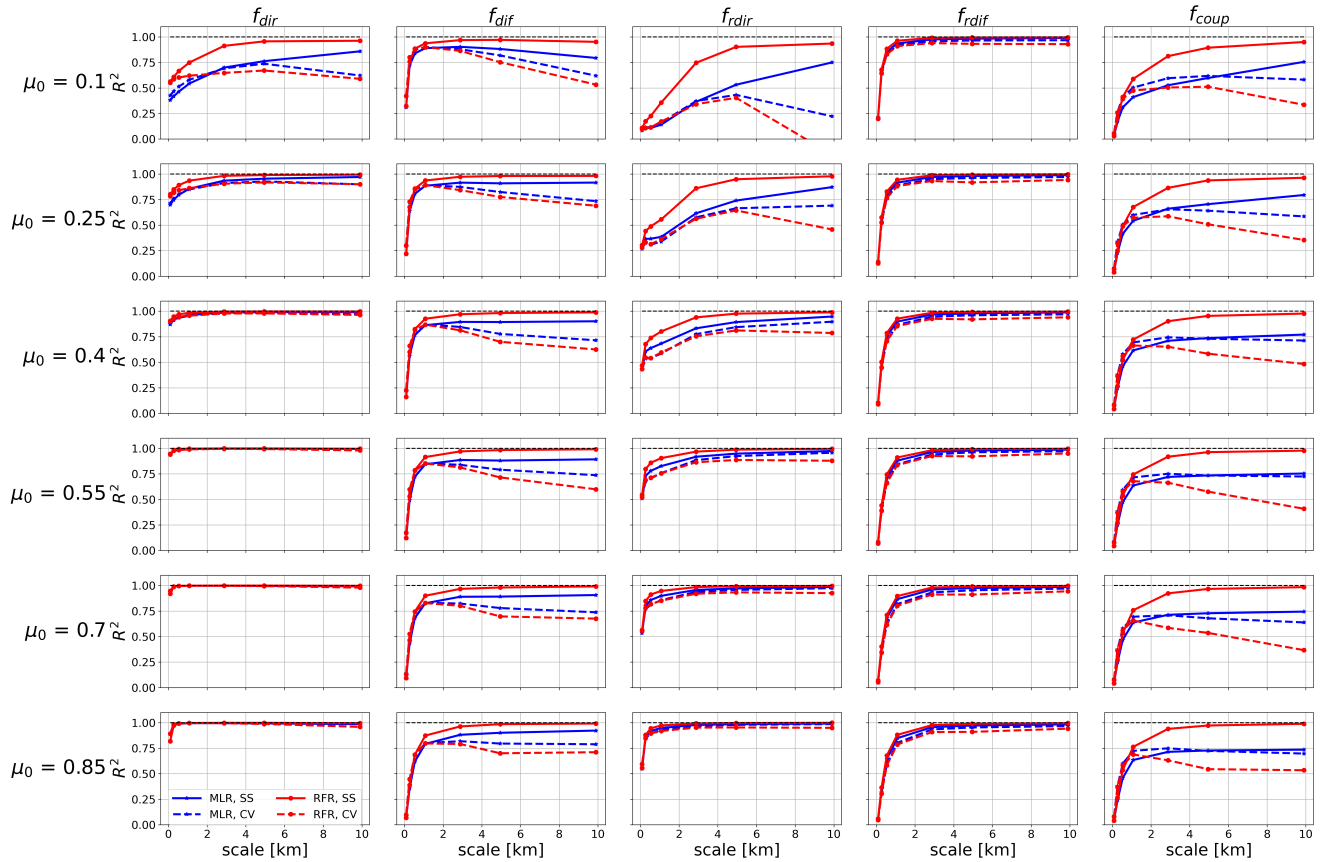
Figure 7. Coefficient of determination R^2 for the two different predictive models: Multiple Linear Regression (MLR, blue lines), and Random Forest Regression (RFR, red lines). Results are reported for varying averaging scales and cosines of the solar zenith angle (μ_0). The models were trained over the Peru site and tested over the same site (SS, continuous lines) and over the independent EastAlps site for cross validation (CV, dashed lines).
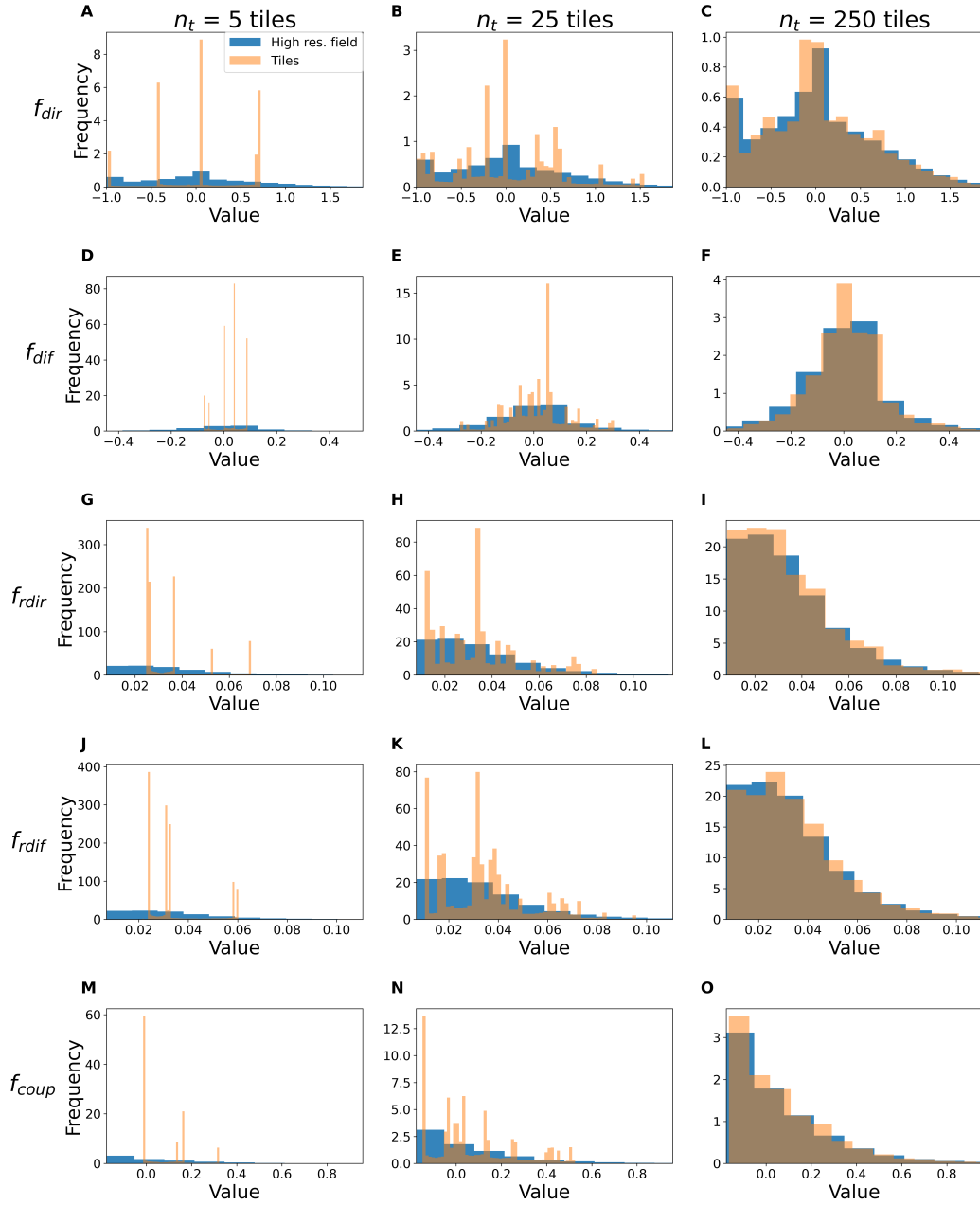
Figure 8. Histograms of the distribution of 3D - PP incident radiation differences for varying number of tiles. Average 3D correction over each tile (orange) are compared with the frequency distribution of the high resolution field (blue histograms). Results are shown for the EastAlps domain, for a given solar angle ($\mu_0 = 0.4$)
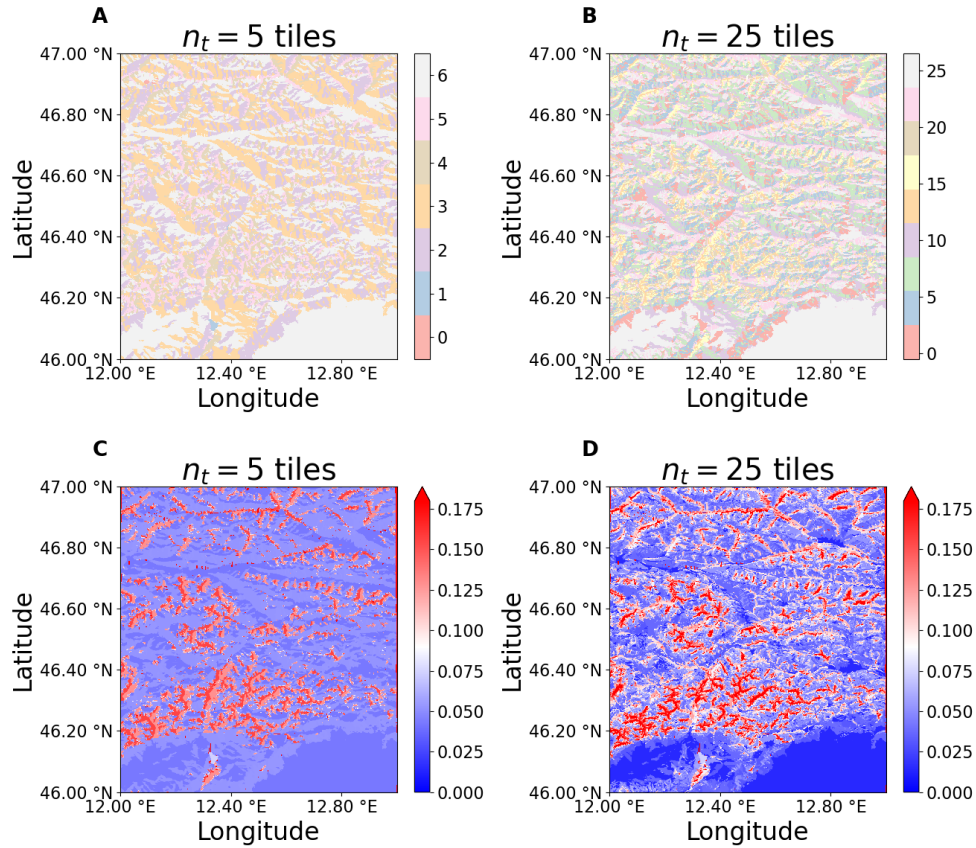
Figure 9. Effect of a different number of tiles for modelling the sub-grid variability of the direct flux over the study site. Top panels: spatial distribution of the tiles representing homogeneous land units. Note that for this domain in addition to the n_t tiles part of land hillslopes there are two additional tiles corresponding respectively to glaciers (tile 0) and lakes (tile 1) so that the effective number of tiles is 7 and 27 for panels (A) and (B). Bottom panel: spatial distribution of the terrain view factor $\tilde{C}_t$ local average evaluate over each tile.
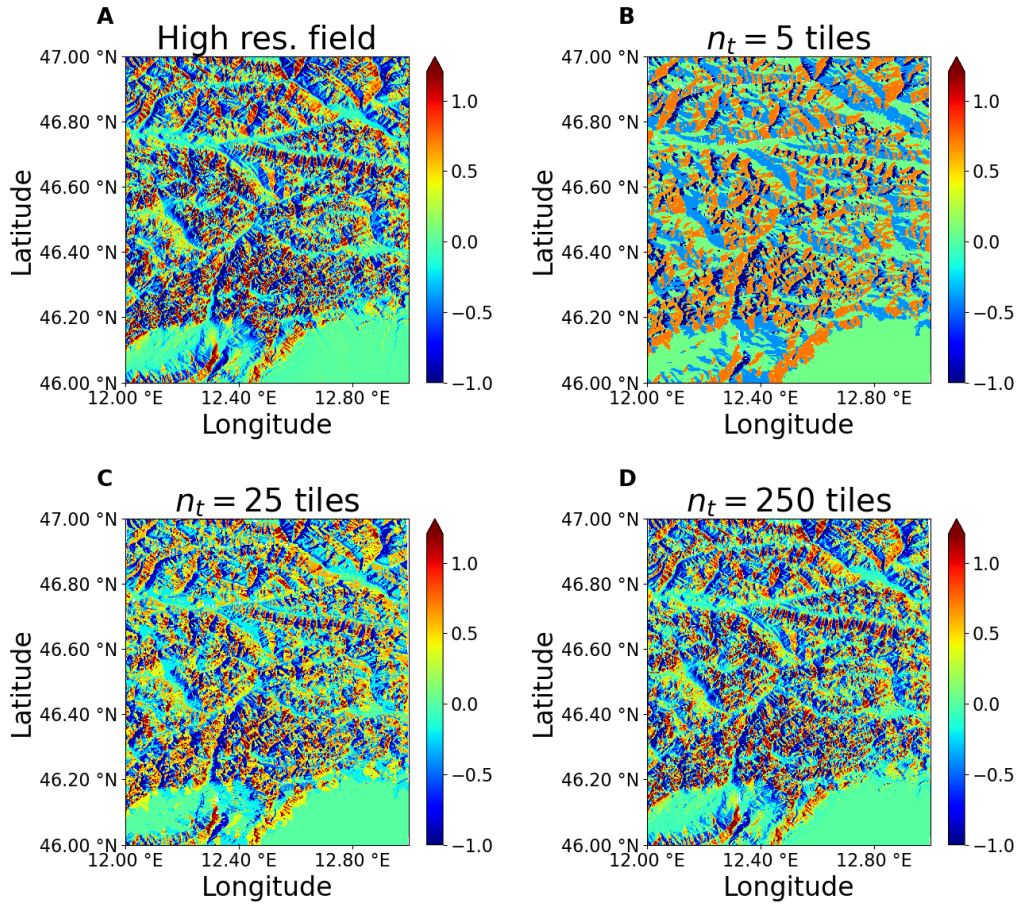
Figure 10. Normalized differences between 3D and PP direct fluxes for high resolution predictions and predictions for different numbers of tiles ($k = 5, 25, 250$), obtained setting a fixed number of hillslopes and varying the number of units for each hillslope ($k = 5$).
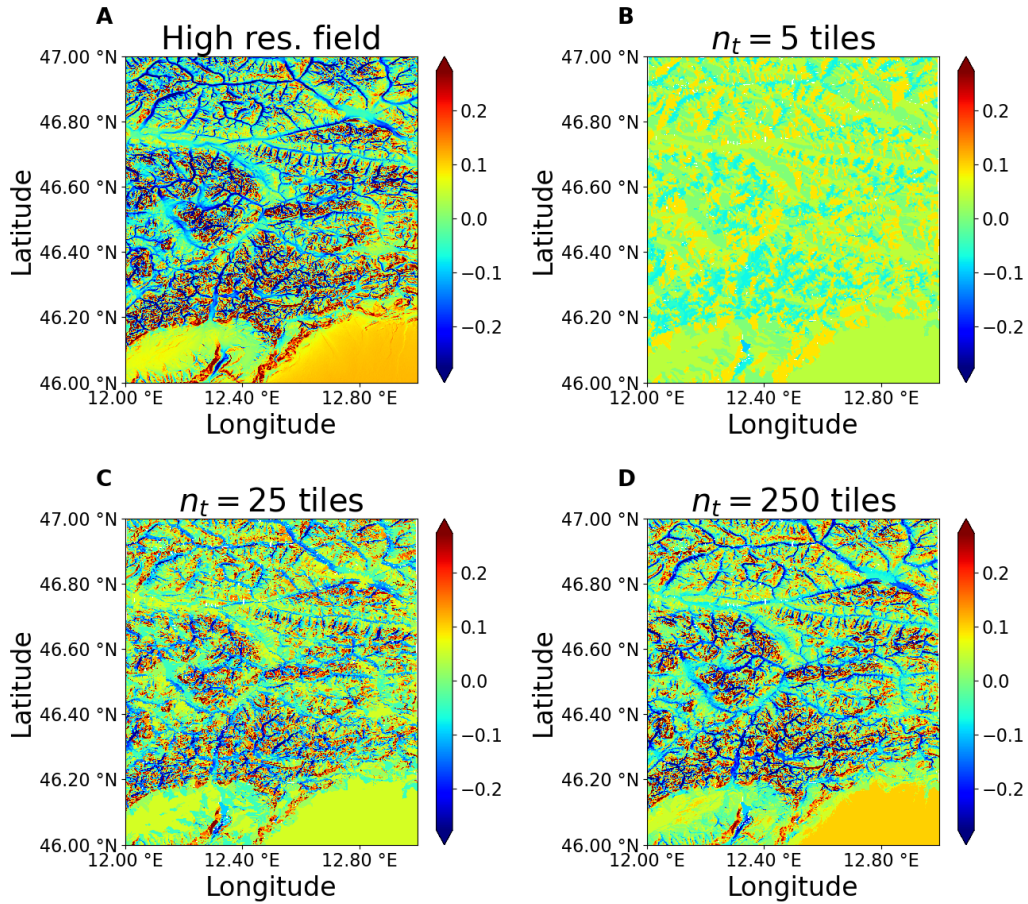
Figure 11. Normalized differences between 3D and PP diffuse fluxes for high resolution predictions and predictions for different numbers of hillslopes ($k = 5, 25, 250$) setting a fixed number of tiles / hillslope ($k = 5$).
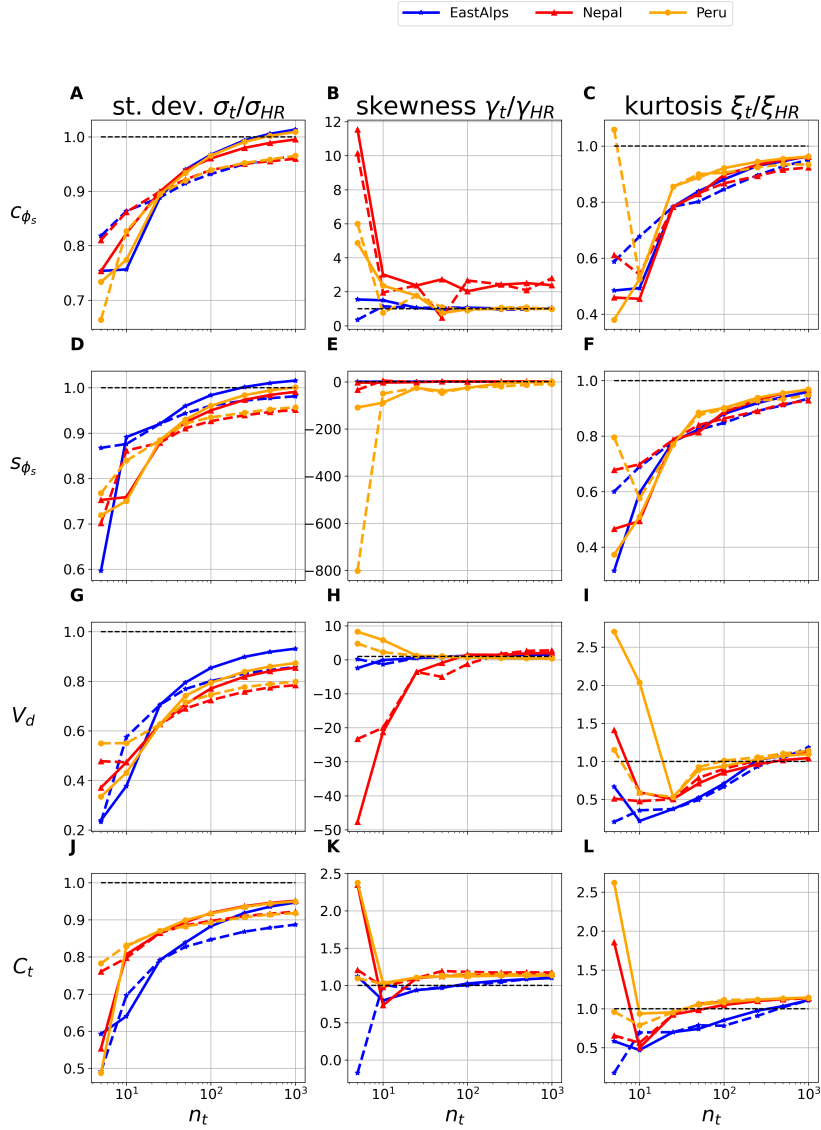
Figure 12. Convergence to the high resolution terrain properties (slope orientation, sky view and terrain view) obtained by increasing the number of tiles used in the parameterization. Two different tiling schemes are shown, respectively obtained fixing the number of hillslopes ($k = 5$) and varying that of sub-grid units p (continuous lines), or fixing $p = 5$ and varying k (dashed lines). Results are reported for terrain variables.
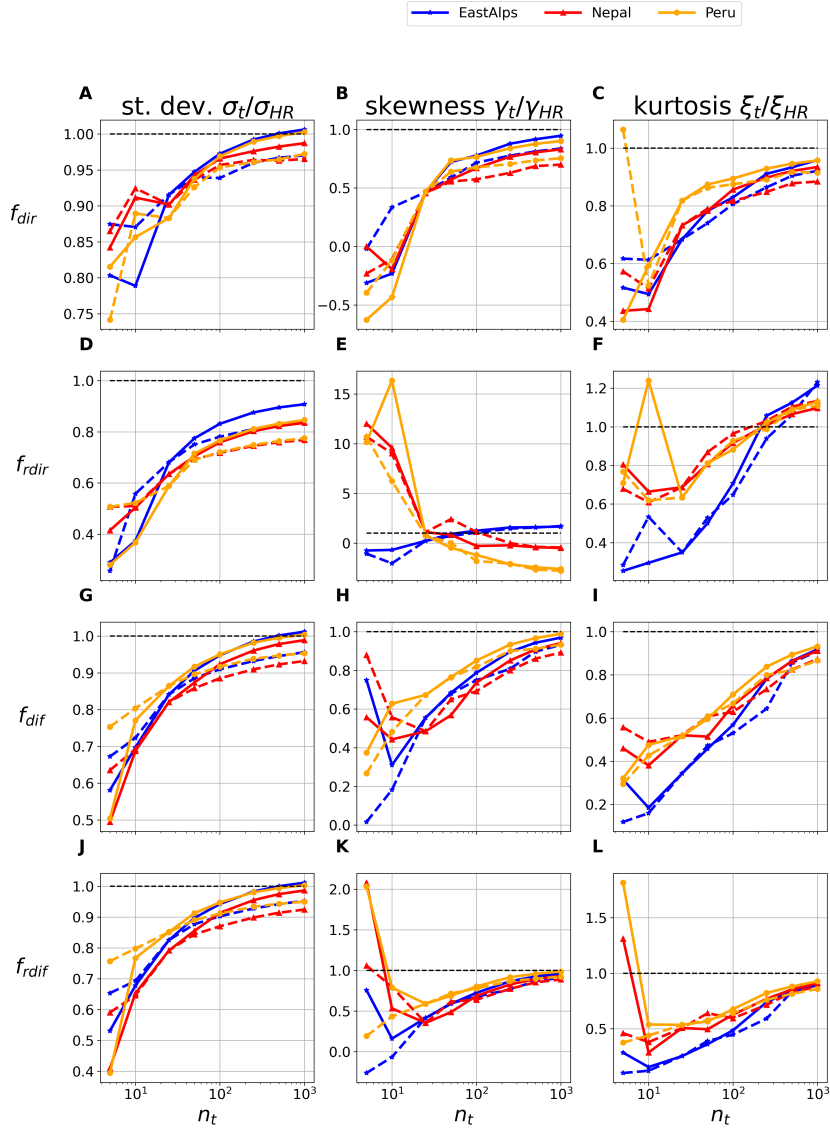
Figure 13. Convergence to the high resolution radiation fields (direct, diffuse, reflected-direct and reflected-diffuse differences between 3D and PP cases). Results are obtained by increasing the number of tiles used in the parameterization. Two different tiling schemes are shown, respectively obtained fixing the number of hillslopes ($k = 5$) and varying that of sub-grid units p (continuous lines), or fixing $p = 5$ and varying k (dashed lines). Results are reported for flux normalized differences.
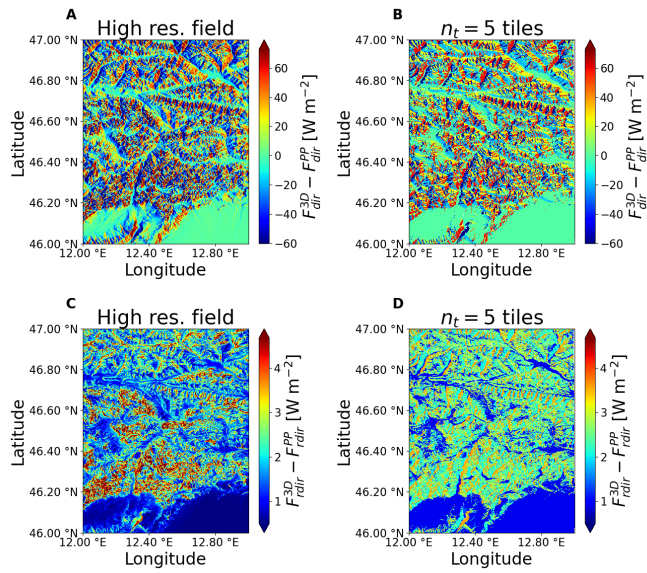
Figure 14. Downward radiation differences between 3D and PP fluxes for high resolution predictions (left column) and predictions and for 5 tiles (right column) for each flux component. Results are shown for a representative case of clear sky conditions and $cos\theta_0 = 0.4$ for direct flux (top panels) and reflected-directed flux (bottom).
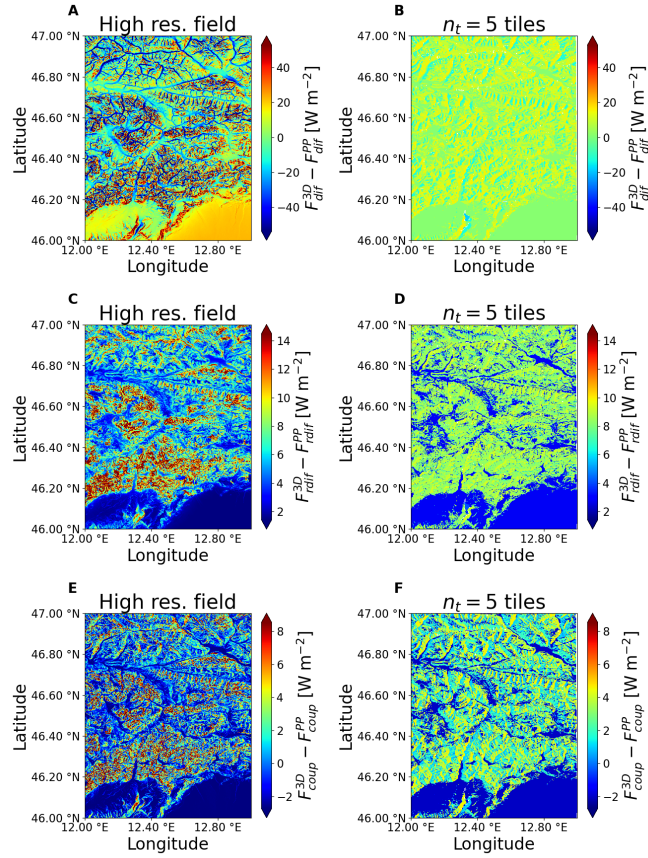
Figure 15. Same as figure 14 for diffuse, reflected-diffuse and coupled flux components.
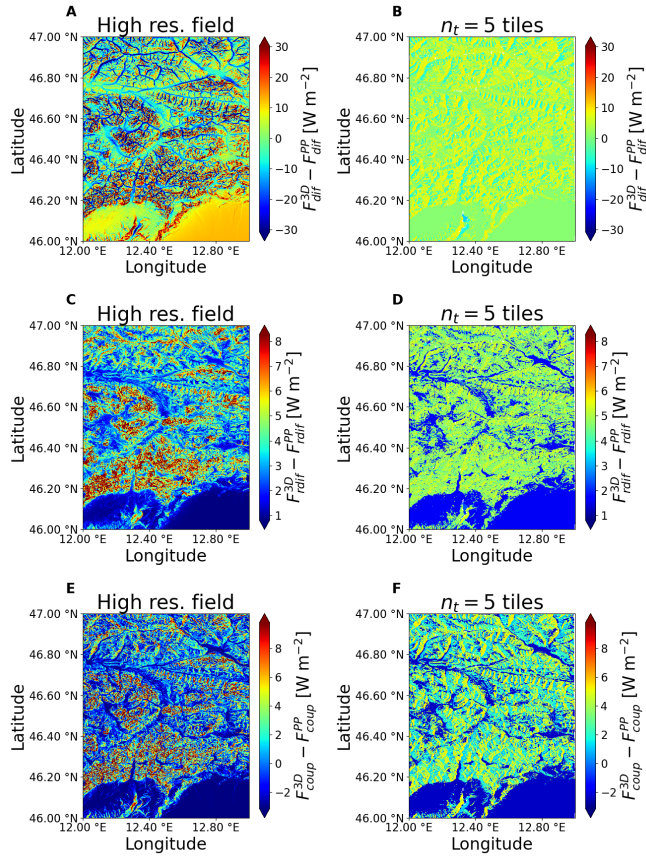
Figure 16. Downward radiation differences between 3D and PP fluxes for high resolution predictions (left column) and predictions and for 5 tiles (right column) for each flux component. Results are shown for a representative case of cloudy sky conditions and and $cos\theta_0 = 0.4$. Direct and reflected direct fluxes are zero in this case.
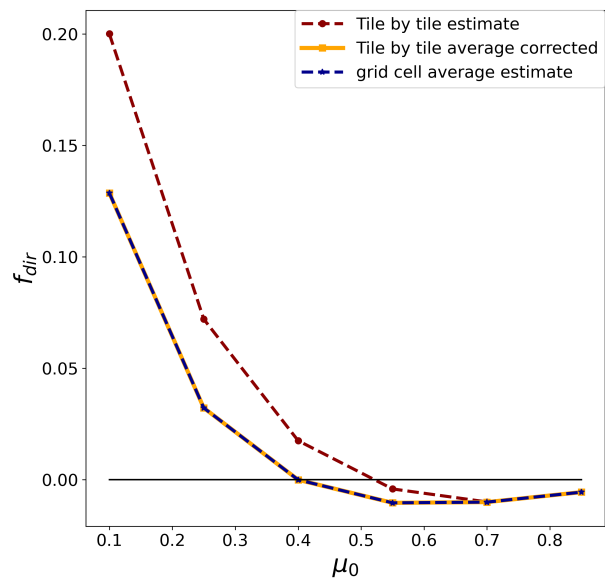
Figure 17. Comparison between grid average estimates of f_{dir} obtained by averaging the tile-by-tile corrections, and by applying the predictive model for f_{dir} to the grid-cell average terrain parameter predictors. Results are shown for the EastAlps site for μ_0 varying from 0.1 to 0.85, and solar azimuth $\phi = \pi/2$.